

# A new anisotropic bending model for nonlinear shells: Comparison with existing models and isogeometric finite element implementation

Eshwar J. Savitha<sup>a</sup> and Roger A. Sauer<sup>a,b,c,\*</sup>

<sup>a</sup>*Aachen Institute for Advanced Study in Computational Engineering Science (AICES),  
RWTH Aachen University, Templergraben 55, 52056 Aachen, Germany*

<sup>b</sup>*Faculty of Civil and Environmental Engineering, Gdańsk University of Technology, ul. Narutowicza  
11/12, 80-233 Gdańsk, Poland*

<sup>c</sup>*Dept. of Mechanical Engineering, Indian Institute of Technology Guwahati, Assam 781039, India*

**Abstract:** A new nonlinear hyperelastic bending model for shells formulated directly in surface form is presented, and compared to four prominently used bending models. Through an essential set of elementary nonlinear bending test cases, the stresses and moments of each model are examined analytically. Only the proposed bending model passes all the test cases while the other bending models either fail or only pass the test cases for small deformations. The proposed new bending model can handle large deformations and initially curved surfaces. It is based on the principal curvatures and their directions in the initial configuration, and it thus can have different bending moduli along those directions. These characteristics make it flexible in modeling a given material, while it does not suffer from the pathologies of existing bending models. Further, the bending models are compared computationally through four classical benchmark examples and one contact example. As the underlying shell theory is based on Kirchhoff-Love kinematics, isogeometric NURBS shape functions are used to discretize the shell surface. The linearization and efficient finite element implementation of the proposed new model are also provided.

**Keywords:** Kirchhoff-Love shells, direct shell formulation, curvilinear coordinates, nonlinear finite elements, isogeometric analysis, bending models

## 1 Introduction

Shells are curved thin-walled structures appearing in nature and engineering designs. The curvature enables shells to be designed with high load-bearing capacity at minimal use of materials. This high strength-to-weight ratio makes them ubiquitous in many applications. Extensive efforts have been made to accurately describe the load-carrying behavior of shells. The finite element method (FEM) is the predominantly used numerical technique to solve shell problems. It is common practice in FEM formulations of slender structures such as plates, membranes, and shells, to reduce the dimension from volume to surface. This significantly simplifies the numerical discretization, reduces the degrees-of-freedom (dofs), and condenses the 3D kinematics to 2D. Savings in computational time naturally follow.

The three mainly used ways of dimensionality reduction are derived, degenerate, and direct surface approaches (Bischoff et al., 2004). In the derived approach, an approximate shell theory is derived by asymptotic (analytical or numerical) integration of the 3D equations. Some examples of the early works, which mainly focused on linear theories, are those by Gol'denveizer (1963), Reissner (1963) and Cicala (1965). In the degenerate solid approach, the shell behavior

\*corresponding author, email: roger.sauer@pg.edu.pl, sauer@aices.rwth-aachen.de

is obtained by reducing or degenerating 3D continuum mechanics through kinematic assumptions. This was first developed by [Ahmad et al. \(1970\)](#) and a comprehensive presentation of the methodology can be found in [Hughes \(2012\)](#). In the direct surface approach, only the shell surface is considered *ab initio* and well-defined constitutive laws are proposed to obtain stresses and moments. The underlying theory of this method goes back to [Cosserat \(1909\)](#). This was followed by prominent works of [Ericksen and Truesdell \(1957\)](#), [Green et al. \(1965\)](#), [Naghdi \(1973\)](#) and [Simo et al. \(1990\)](#).

In solid mechanics, nonlinearities arise from the material behavior and the geometry of large deformations. Some early works on the theory of nonlinear analysis of shells was given by [Novozhilov \(1953\)](#) and [Pietraszkiewicz \(1989\)](#). Computational aspects of nonlinear shell modeling were presented in [Hughes and Liu \(1981\)](#); [Dvorkin and Bathe \(1984\)](#); [Simo et al. \(1990\)](#); [Betsch et al. \(1996\)](#). There are also several nonlinear shell formulations put forth for the modeling of soft materials such as rubbers ([Chróscielewski et al., 1992](#); [Başar and Itskov, 1998](#)), tissues ([Itskov, 2001](#); [Pandolfi and Manganiello, 2006](#); [Prot et al., 2007](#)), red blood cells ([Dao et al., 2003](#); [Mills et al., 2004](#)), lipid bilayers ([Steigmann, 1999](#); [Feng and Klug, 2006](#)) and viscoelastic materials ([Evans and Hochmuth, 1976](#); [Neff, 2005](#)).

In addition to the dimensionality reduction, the underlying shell kinematics also plays a vital role in constructing shell theories. The two widely used shell theories are Reissner-Mindlin (RM) ([Reissner, 1945](#); [Mindlin, 1951](#)) and Kirchhoff-Love (KL) ([Kirchhoff, 1850](#); [Love, 1888](#)). In KL theory the cross-section remains normal to the mid surface during deformation, whereas in RM shell theory, a shear angle can appear. Therefore, RM theory has both displacement and rotational degrees-of-freedom (dofs), and  $C^0$ -continuous shape functions suffice for discretization. On the other hand, KL theory has only displacement dofs. It therefore accommodates bending in the governing equations through displacements itself. This results in a fourth-order strong form equation for KL shells. The corresponding principle of virtual work contains second order derivatives which necessitates  $C^1$ -continuous shape functions for discretization. There are several methods developed to enforce  $C^1$ -continuity for Lagrange shape functions like rotation-free elements ([Oñate and Zárate, 2000](#); [Brunet and Sabourin, 2006](#)), discontinuous Galerkin formulation ([Noels and Radovitzky, 2008](#)) and mesh-free methods ([Krysl and Belytschko, 1996](#)). However, these methods are usually complex and/or expensive. Therefore RM based shells are commonly used in commercial finite element (FE) codes as they can be used with simple classical Lagrange shape functions.

A new approach to obtain  $C^1$ -continuous shape function called Isogeometric analysis (IGA) was introduced by [Hughes et al. \(2005\)](#). There the spline-based basis functions used to create the geometry, such as B-splines or Non-Uniform Rational B-Splines (NURBS), itself are used for the FE analysis. The Bézier extraction operator developed by [Borden et al. \(2011\)](#) enabled a NURBS surface to be decomposed into Bézier elements to seamlessly incorporate isogeometric analysis into existing FE code. The advantages of IGA over conventional approaches in shell problems were shown by [Kiendl et al. \(2009\)](#) for KL and [Benson et al. \(2010\)](#) for RM shells. A KL shell formulation doesn't just benefit from having fewer dofs compared to a RM shell, but it is also shear locking free. However, both KL and RM shells suffer from membrane-bending locking. This type of locking arises due to the undesirable coupling of membrane and bending modes. A variety of solutions exists for alleviating membrane-bending locking in IGA shells, such as reduced quadrature ([Adam et al., 2015](#); [Zou et al., 2021](#)), mixed formulations ([Bieber et al., 2018](#)) and assumed natural strain methods ([Caseiro et al., 2014](#)). [Kiendl et al. \(2015\)](#) presented an isogeometric KL shell formulation such that an arbitrary 3D constitutive models can be used. Along similar lines, [Duong et al. \(2017\)](#) proposed a formulation that admits constitutive laws obtained by thickness-integration of 3D material models as well as those constructed directly in surface energy form. IGA shell formulations have been applied to the study of rubbers ([Taylor,](#)

2011; Elguedj and Hughes, 2014), tissues (Tepole et al., 2015; Roohbakhshan and Sauer, 2017), red blood cells (Casquero et al., 2017; Barthezzi et al., 2019), lipid bilayers (Sauer et al., 2017; Audyya et al., 2021) and viscoelastic materials (Dortdivanlioglu and Javili, 2021; Paul and Sauer, 2022). IGA shells have also been used in inverse problems such as shape optimization (Kiendl et al., 2014) and material reconstruction (Borzeszkowski et al., 2022).

One of the material models for the direct surface approach was proposed by Koiter (1966). It is a linear relation between certain strains and stresses that can be derived from thickness integration of the 3D St.Venant-Kirchhoff material model. The Koiter model was later extended by Steigmann (2012) to materials exhibiting arbitrary symmetry. A comprehensive derivation can also be found in Steigmann (2013). Two other direct surface material model were proposed by Canham (1970a), to study red blood cells, and Helfrich (1973), to study the elastic properties of lipid bilayers. The Helfrich model, which includes the Canham model as a special case, is one of most widely used material models in morphological studies of the vesicles, which are closed bilayer films.

KL shell formulations are primarily used with bending models derived from 3D or directly proposed for the surface such as the Koiter and Helfrich model. There aren't many examples of direct bending models besides those of Koiter and Helfrich. As is shown here, these suffer from an inability to handle nonlinear deformations or initially stress-free curved surfaces. We address these shortcomings by proposing a new nonlinear anisotropic bending model for the direct surface formulation of shells. It is motivated by eliminating the *physical* stretch-dependency on bending that is affecting existing bending models at large deformations. This is different from treating membrane-bending locking, which is caused by a *numerical* stretch-dependency of bending of very thin shells that is already a problem at small deformations. Membrane-bending locking is due to shortcomings in the underlying finite element discretization and therefore needs to be treated at that level, as was noted above. Our concern is purely physical and therefore needs to be treated at the constitutive level. Our description uses a direct surface formulation for KL shells in curvilinear coordinates together with an isogeometric surface discretization, which is very general and accurate, yet straightforward to implement (Duong et al., 2017).

The salient features of the proposed new bending model are:

- It is objective, admits large deformations and captures anisotropic bending.
- It allows to describe initially curved stress-free shells.
- It offers great flexibility in modeling a given material.
- It is compared to existing bending models and it agrees with those at small deformations.
- In contrast to existing models, it passes a proposed set of nonlinear bending test cases.
- It allows for an efficient implementation within isogeometric shell FE.

The remainder of this paper is organized as follows: Sec. 2 provides an overview of general thin shell theory in curvilinear coordinates. In Sec. 3, existing bending models are presented along with the proposed new bending model. In Sec. 4, these models are then compared and their shortcomings are illustrated using five analytical test cases. In Sec. 5, the new bending model is examined in several numerical examples. The paper concludes with Sec. 6.

## 2 Thin-shell formulation

This section summarizes the Kirchhoff-Love thin-shell theory formulation of [Sauer and Duong \(2017\)](#) and [Duong et al. \(2017\)](#) that is based on curvilinear coordinates and isogeometric finite elements. First, the essential kinematical relations, governing strong and weak form equations, and hyperelastic constitutive equations are introduced in Sec. 2.1-2.3. Then, the linearization and finite element approximation of the resulting nonlinear equations are presented in Sec. 2.4 and 2.5.

### 2.1 Surface kinematics

The current and initial configuration of a shell surface embedded within 3D space can be parametrized respectively as

$$\mathbf{x} = \mathbf{x}(\xi^\alpha), \quad \text{and} \quad \mathbf{X} = \mathbf{X}(\xi^\alpha), \quad (1)$$

with parameters  $\xi^1$  and  $\xi^2$ . A basis in the curvilinear setting can then be defined by a pair of covariant tangent vectors ( $\mathbf{a}_\alpha$ ,  $\alpha = 1, 2$ ) and normal ( $\mathbf{n}$ ) as

$$\mathbf{a}_\alpha := \frac{\partial \mathbf{x}}{\partial \xi^\alpha}, \quad \mathbf{n} := \frac{\mathbf{a}_1 \times \mathbf{a}_2}{\|\mathbf{a}_1 \times \mathbf{a}_2\|}. \quad (2)$$

A similar set of basis vectors is defined for the initial configuration as

$$\mathbf{A}_\alpha := \frac{\partial \mathbf{X}}{\partial \xi^\alpha}, \quad \mathbf{N} := \frac{\mathbf{A}_1 \times \mathbf{A}_2}{\|\mathbf{A}_1 \times \mathbf{A}_2\|}. \quad (3)$$

Since the covariant tangent vectors are not orthogonal, i.e. the covariant surface metric  $a_{\alpha\beta} = \mathbf{a}_\alpha \cdot \mathbf{a}_\beta \neq 0$ , its dual vectors are introduced by

$$\mathbf{a}^\alpha := a^{\alpha\beta} \mathbf{a}_\beta, \quad (4)$$

such that  $\mathbf{a}_\alpha \cdot \mathbf{a}^\beta = \delta_\alpha^\beta$  and  $[a^{\alpha\beta}] := [a_{\alpha\beta}]^{-1}$ . The surface stretch is given by  $J = \sqrt{J_a/J_A}$  where  $J_a := \|\mathbf{a}_1 \times \mathbf{a}_2\|$  and  $J_A := \|\mathbf{A}_1 \times \mathbf{A}_2\|$  is the area of the parallelogram enclosed by the covariant tangents in the current and initial configuration, respectively. The components of the surface curvature can be defined as

$$b_{\alpha\beta} := \mathbf{a}_{\alpha,\beta} \cdot \mathbf{n}, \quad b_\beta^\alpha := a^{\alpha\gamma} b_{\gamma\beta}, \quad \text{and} \quad b^{\alpha\beta} := b_\gamma^\alpha a^{\gamma\beta}. \quad (5)$$

Analogous curvature definitions, denoted  $B^{\alpha\beta}$ ,  $B_\beta^\alpha$  and  $B^{\alpha\beta}$ , follow for the initial configuration. The two invariants of the curvature tensor,  $\mathbf{b} = b_{\alpha\beta} \mathbf{a}^\alpha \otimes \mathbf{a}^\beta$ , called mean and Gaussian curvature are calculated respectively as

$$H := \frac{1}{2} \text{tr } \mathbf{b} = \frac{1}{2} b_\alpha^\alpha = \frac{1}{2} a^{\alpha\beta} b_{\alpha\beta}, \quad (6)$$

$$\kappa := \det \mathbf{b} = \frac{\det[b_{\alpha\beta}]}{\det[a_{\alpha\beta}]}.$$

The principal curvature of the surface can then be calculated as

$$\kappa_{1/2}^* = H \pm \sqrt{H^2 - \kappa}. \quad (8)$$

Additionally, we define two symmetric tensors: The Green-Lagrange strain tensor,

$$\mathbf{E} = \varepsilon_{\alpha\beta} \mathbf{A}^\alpha \otimes \mathbf{A}^\beta := \frac{1}{2} (a_{\alpha\beta} - A_{\alpha\beta}) \mathbf{A}^\alpha \otimes \mathbf{A}^\beta, \quad (9)$$

and the relative curvature tensor,

$$\mathbf{K} = K_{\alpha\beta} \mathbf{A}^\alpha \otimes \mathbf{A}^\beta := (b_{\alpha\beta} - B_{\alpha\beta}) \mathbf{A}^\alpha \otimes \mathbf{A}^\beta. \quad (10)$$

A more detailed description of thin shell kinematics and its variation can be found for example in [Sauer \(2018\)](#).

## 2.2 Strong form and weak form

The quasi-static shell boundary value problem governs the displacement field  $\mathbf{u}$  of the surface  $\mathcal{S}$  through the fourth order partial differential equation

$$\mathbf{T}_{;\alpha}^\alpha + \mathbf{f} = \mathbf{0} \quad \forall \mathbf{x} \in \mathcal{S}, \quad (11)$$

where  $\mathbf{f}$  is a body force on  $\mathcal{S}$ , and the prescribed displacement ( $\bar{\mathbf{u}}$ ), traction ( $\bar{\mathbf{t}}$ ), and bending moment ( $\bar{m}_\tau$ ) boundary conditions

$$\mathbf{u} = \bar{\mathbf{u}} \quad \text{on } \partial_u \mathcal{S}, \quad (12)$$

$$\mathbf{t} = \bar{\mathbf{t}} \quad \text{on } \partial_t \mathcal{S}, \quad (13)$$

$$m_\tau = \bar{m}_\tau \quad \text{on } \partial_m \mathcal{S}. \quad (14)$$

In Eq. (11),

$$\mathbf{T}^\alpha = N^{\alpha\beta} \mathbf{a}_\beta + S^\alpha \mathbf{n} \quad (15)$$

is the stress vector. Here,  $N^{\alpha\beta}$  and  $S^\alpha$  are the in-plane membrane and the out-of-plane shear stress components defined via Cauchy's theorem. From angular momentum balance follows

$$\begin{aligned} \sigma^{\alpha\beta} &:= N^{\alpha\beta} - b_\gamma^\beta M^{\gamma\alpha} = \sigma^{\beta\alpha}, \\ S^\alpha &= -M_{;\beta}^{\beta\alpha}, \end{aligned} \quad (16)$$

where  $M^{\alpha\beta}$  are the stress couples caused by out-of-plane bending. Tab. 1 gives an overview of the different stress components. As shown, they can be either expressed per current surface area or per reference surface area.

	per current area	per reference area
physical membrane stress	$N^{\alpha\beta} = \sigma^{\alpha\beta} + b_\gamma^\alpha M^{\gamma\beta}$	$N_0^{\alpha\beta} = J N^{\alpha\beta}$
effective membrane stress	$\sigma^{\alpha\beta} = \frac{2}{J} \frac{\partial W}{\partial a_{\alpha\beta}}$	$\tau^{\alpha\beta} = J \sigma^{\alpha\beta}$
bending stress couple	$M^{\alpha\beta} = \frac{1}{J} \frac{\partial W}{\partial b_{\alpha\beta}}$	$M_0^{\alpha\beta} = J M^{\alpha\beta}$
out-of-plane shear stress	$S^\alpha = -M_{;\beta}^{\beta\alpha}$	$S_0^\alpha = J S^\alpha$

**Table 1:** Different stress components w.r.t. the current or reference configuration.  $N^{\alpha\beta}$  is the Cauchy membrane stress appearing in the strong form equilibrium equation (11), while the effective stress  $\sigma^{\alpha\beta}$  appears in the weak form. Their transformation to the reference configuration correspond to Kirchhoff membrane stresses.

Multiplying strong form Eq. (11) with a suitable variation  $\delta \mathbf{x} \in \mathcal{V}$  and integrating it over surface  $\mathcal{S}$ , leads to the weak form

$$G_{\text{int}} - G_{\text{ext}} = 0 \quad \forall \delta \mathbf{x} \in \mathcal{V}, \quad (17)$$

where

$$G_{\text{int}} = \int_{\mathcal{S}_0} \delta \varepsilon_{\alpha\beta} \tau^{\alpha\beta} dA + \int_{\mathcal{S}_0} \delta b_{\alpha\beta} M_0^{\alpha\beta} dA, \quad (18)$$

$$G_{\text{ext}} = \int_{\mathcal{S}} \delta \mathbf{x} \cdot \mathbf{f} da + \int_{\partial_t \mathcal{S}} \delta \mathbf{x} \cdot \mathbf{t} ds + \int_{\partial_m \mathcal{S}} \delta \mathbf{n} \cdot m_\tau \boldsymbol{\nu} ds. \quad (19)$$

Eq. (18) contains the virtual work of the in-plane membrane deformations and out-of-plane bending deformations. It can be extended to out-of-plane shear and strain deformations (Simo et al., 1990) and in-plane bending deformations (Steigmann, 2018; Duong et al., 2020) in the context of more general shell theories. The last part of Eq. (19) represents the virtual work of moment  $m_\tau \boldsymbol{\nu}$ , with  $\boldsymbol{\nu}$  being the normal to the boundary where bending moment  $m_\tau$  is applied.

### 2.3 Surface Hyperelasticity

For hyperelastic materials, the membrane stress and the moment components in weak form (17) are calculated from the surface energy density  $W$  (with units [J/m<sup>2</sup>]) by

$$\begin{aligned} \tau^{\alpha\beta} &= 2 \frac{\partial W}{\partial a_{\alpha\beta}}, \\ M_0^{\alpha\beta} &= \frac{\partial W}{\partial b_{\alpha\beta}}. \end{aligned} \quad (20)$$

It is convenient to decompose the surface energy density into two parts,

$$W = W_m + W_b, \quad (21)$$

associated with membrane and bending deformations. Ideally, the former should only generate membrane stresses, while the latter only generates bending stresses. However this is not possible in the case of coupled membrane-bending material behavior. We proceed by introducing some simple hyperelastic membrane models below. Hyperelastic bending models are then discussed in detail in Sec. 3.

An example of a linear elastic membrane strain energy is the Koiter model. Its membrane strain energy is of the form

$$W_{\text{mKo}} = \frac{1}{2} \mathbf{E} : \mathbb{C} : \mathbf{E}, \quad (22)$$

where the fourth order tensor  $\mathbb{C}$  is defined as

$$\mathbb{C} = \Lambda \mathbf{I} \odot \mathbf{I} + 2\mu (\mathbf{I} \otimes \mathbf{I})^s. \quad (23)$$

Here,  $\Lambda$  and  $\mu$  are the surface Lamé parameters (with units [N/m]). Inserting Eq. (23) into (22) leads to

$$W_{\text{mKo}} = \frac{1}{2} \left( \Lambda (\text{tr} \mathbf{E})^2 + 2\mu E_{\alpha\beta} E^{\alpha\beta} \right), \quad (24)$$

where

$$\text{tr} \mathbf{E} = E^{\alpha\beta} A_{\alpha\beta}, \quad \text{and} \quad E^{\alpha\beta} := A^{\alpha\gamma} E_{\gamma\delta} A^{\delta\beta}. \quad (25)$$

The Kirchhoff stress and in-plane moment contributions of the Koiter membrane model are obtained from Eq. (20) as

$$\begin{aligned}\tau_{\text{mKo}}^{\alpha\beta} &= \Lambda \text{tr } \mathbf{E} A^{\alpha\beta} + 2\mu E^{\alpha\beta}, \\ M_{0\text{mKo}}^{\alpha\beta} &= 0.\end{aligned}\quad (26)$$

Another commonly used membrane model, which can be derived from 3D elasticity, is the Neo-Hookean surface model. Its strain energy function can be written as

$$W_{\text{mNH}} = \frac{\Lambda}{4} (J^2 - 1 - 2 \ln J) + \frac{\mu}{2} (I_1 - 2 - 2 \ln J). \quad (27)$$

Here,  $I_1 = A^{\alpha\beta} a_{\alpha\beta}$  is the first invariant of the surface Cauchy-Green tensors. The Neo-Hookean model only produces the membrane stress

$$\tau_{\text{mNH}}^{\alpha\beta} = \frac{\Lambda}{2} (J^2 - 1) a^{\alpha\beta} + \mu (A^{\alpha\beta} - a^{\alpha\beta}), \quad (28)$$

i.e.  $M_{0\text{mNH}}^{\alpha\beta} = 0$ .

## 2.4 Linearization

In order to solve the nonlinear Eq. (17) using the Newton-Raphson method, its linearization is necessary. This leads to the increment for the internal virtual work

$$\Delta G_{\text{int}} = \int_{\mathcal{S}_o} \left( c^{\alpha\beta\gamma\delta} \delta\varepsilon_{\alpha\beta} \Delta\varepsilon_{\gamma\delta} + d^{\alpha\beta\gamma\delta} \delta\varepsilon_{\alpha\beta} \Delta b_{\gamma\delta} + \tau^{\alpha\beta} \Delta\delta\varepsilon_{\alpha\beta} + e^{\alpha\beta\gamma\delta} \delta b_{\alpha\beta} \Delta\varepsilon_{\gamma\delta} + f^{\alpha\beta\gamma\delta} \delta b_{\alpha\beta} \Delta b_{\gamma\delta} + M_0^{\alpha\beta} \Delta\delta b_{\alpha\beta} \right) dA, \quad (29)$$

where the material tangents are defined as

$$\begin{aligned}c^{\alpha\beta\gamma\delta} &:= \frac{\partial \tau^{\alpha\beta}}{\partial \varepsilon_{\gamma\delta}}, & d^{\alpha\beta\gamma\delta} &:= \frac{\partial \tau^{\alpha\beta}}{\partial b_{\gamma\delta}}, \\ e^{\alpha\beta\gamma\delta} &:= \frac{\partial M_0^{\alpha\beta}}{\partial \varepsilon_{\gamma\delta}}, & f^{\alpha\beta\gamma\delta} &:= \frac{\partial M_0^{\alpha\beta}}{\partial b_{\gamma\delta}}.\end{aligned}\quad (30)$$

Examples for these, along with  $\Delta\varepsilon_{\alpha\beta}$  and  $\Delta b_{\alpha\beta}$  can be found in [Sauer \(2018\)](#).

## 2.5 Isogeometric FE approximation

The geometry within an undeformed finite element  $\Omega_0^e$  and its deformed counterpart  $\Omega^e$  is interpolated from the positions of control points  $\mathbf{X}_e$  and  $\mathbf{x}_e$ , respectively, as

$$\mathbf{X} = \mathbf{N}_e \mathbf{X}_e, \quad \mathbf{x} = \mathbf{N}_e \mathbf{x}_e, \quad (31)$$

with

$$\mathbf{N}_e(\xi^\alpha) := [N_1 \mathbf{1}, N_2 \mathbf{1}, \dots, N_{n_e} \mathbf{1}]. \quad (32)$$

Here  $\{N_A(\xi^\alpha)\}_{A=1}^{n_e}$  are the  $n_e$   $C^1$ -continuous NURBS basis functions of  $\Omega^e$ . Such an arrangement results in a direct correspondence between the discretized equations and their implementation in a computer code. Discretizing Eq. (17) gives

$$\sum_{e=1}^{n_{\text{el}}} (G_{\text{int}}^e + G_{\text{ext}}^e) = 0 \quad \forall \delta \mathbf{x}_e \in \mathcal{V}, \quad (33)$$

where  $n_{\text{el}}$  is the number of elements. Based on Eq. (18) and (31), the internal forces due to membrane stress  $\tau^{\alpha\beta}$  and the bending moment  $M_0^{\alpha\beta}$  will be

$$G_{\text{int}}^e = \delta \mathbf{x}_e^T (\mathbf{f}_{\text{int}\tau}^e + \mathbf{f}_{\text{int}M}^e), \quad (34)$$

where

$$\begin{aligned} \mathbf{f}_{\text{int}\tau}^e &:= \int_{\Omega_0^e} \tau^{\alpha\beta} \mathbf{N}_{e,\alpha}^T \mathbf{a}_\beta dA, \\ \mathbf{f}_{\text{int}M}^e &:= \int_{\Omega_0^e} M_0^{\alpha\beta} \mathbf{N}_{e;\alpha\beta}^T \mathbf{n} dA, \end{aligned} \quad (35)$$

and

$$\mathbf{N}_{e;\alpha\beta}^T := \mathbf{N}_{e,\alpha\beta} - \mathbf{\Gamma}_{\alpha\beta}^\gamma \mathbf{N}_{e,\gamma}. \quad (36)$$

Here,  $\mathbf{N}_{e,\alpha}$  and  $\mathbf{N}_{e,\alpha\beta}$  denote the first and second derivatives of  $\mathbf{N}_e$  w.r.t. parameter  $\xi^\alpha$ . Discretizing Eq. (19), the external virtual work follows as

$$G_{\text{ext}}^e = \delta \mathbf{x}_e^T (\mathbf{f}_{\text{ext}o}^e + \mathbf{f}_{\text{ext}t}^e + \mathbf{f}_{\text{ext}m}^e + \mathbf{f}_{\text{ext}p}^e), \quad (37)$$

where the external FE force vectors are

$$\begin{aligned} \mathbf{f}_{\text{ext}o}^e &:= \int_{\Omega_0^e} \mathbf{N}_e^T \mathbf{f}_0 dA, \\ \mathbf{f}_{\text{ext}t}^e &:= \int_{\partial_t \Omega^e} \mathbf{N}_e^T \mathbf{t} ds, \\ \mathbf{f}_{\text{ext}m}^e &:= \int_{\Omega^e} \mathbf{N}_e^T p \mathbf{n} da, \\ \mathbf{f}_{\text{ext}p}^e &:= - \int_{\partial_m \Omega^e} \mathbf{N}_{e,\alpha}^T \nu^\alpha m_\tau \mathbf{n} ds, \end{aligned} \quad (38)$$

for the body force  $\mathbf{f} = \mathbf{f}_0 + p \mathbf{n}$ . Here  $\mathbf{f}_0$  denotes dead loading, while  $p$  denotes an external pressure always acting normal to the surface, and  $\nu = \nu^\alpha \mathbf{a}_\alpha$  denotes the boundary normal on  $\partial\mathcal{S}$ .

Discretizing Eq. (29) gives

$$\Delta G_{\text{int}} = \delta \mathbf{x}_e^T [\mathbf{k}_{\tau\tau}^e + \mathbf{k}_{\tau M}^e + \mathbf{k}_\tau^e + \mathbf{k}_{M\tau}^e + \mathbf{k}_{\tau\tau}^e + \mathbf{k}_M^e] \Delta \mathbf{x}_e, \quad (39)$$

where

$$\begin{aligned} \mathbf{k}_{\tau\tau}^e &:= \int_{\Omega_0^e} c^{\alpha\beta\gamma\delta} \mathbf{N}_{e,\alpha}^T (\mathbf{a}_\beta \otimes \mathbf{a}_\gamma) \mathbf{N}_{e,\delta} dA, \\ \mathbf{k}_{\tau M}^e &:= \int_{\Omega_0^e} d^{\alpha\beta\gamma\delta} \mathbf{N}_{e,\alpha}^T (\mathbf{a}_\beta \otimes \mathbf{n}) \mathbf{N}_{e;\gamma\delta} dA, \\ \mathbf{k}_{M\tau}^e &:= \int_{\Omega_0^e} e^{\alpha\beta\gamma\delta} \mathbf{N}_{e;\alpha\beta}^T (\mathbf{n} \otimes \mathbf{a}_\gamma) \mathbf{N}_{e,\delta} dA, \\ \mathbf{k}_{MM}^e &:= \int_{\Omega_0^e} f^{\alpha\beta\gamma\delta} \mathbf{N}_{e;\alpha\beta}^T (\mathbf{n} \otimes \mathbf{n}) \mathbf{N}_{e;\gamma\delta} dA, \end{aligned} \quad (40)$$

are the material stiffness matrices and

$$\begin{aligned} \mathbf{k}_\tau^e &:= \int_{\Omega_0^e} \mathbf{N}_{e,\alpha}^T \tau^{\alpha\beta} \mathbf{N}_{e,\beta} dA, \\ \mathbf{k}_M^e &= \mathbf{k}_{M1}^e + \mathbf{k}_{M2}^e + (\mathbf{k}_{M2}^e)^T, \end{aligned} \quad (41)$$

with

$$\mathbf{k}_{M1}^e := - \int_{\Omega_0^e} b_{\alpha\beta} M_0^{\alpha\beta} a^{\gamma\delta} \mathbf{N}_{e,\gamma}^T (\mathbf{n} \otimes \mathbf{n}) \mathbf{N}_{e,\delta} dA, \quad (42)$$

$$\mathbf{k}_{M2}^e := - \int_{\Omega_0^e} M_0^{\alpha\beta} \mathbf{N}_{e,\gamma}^T (\mathbf{n} \otimes \mathbf{a}^\gamma) \tilde{\mathbf{N}}_{e;\alpha\beta} dA, \quad (43)$$

are the geometric stiffness matrices. The discretization of Eq. (38) leads to

$$\Delta G_e^e = \delta \mathbf{x}_e^T (\mathbf{k}_{\text{extp}}^e + \mathbf{k}_{\text{extm}}^e) \Delta \mathbf{x}_e, \quad (44)$$

where  $\mathbf{k}_{\text{extp}}^e$  and  $\mathbf{k}_{\text{extm}}^e$  can be found in [Sauer et al. \(2014\)](#) and [Duong et al. \(2017\)](#), respectively.

### 3 Bending constitution

This section presents hyperelastic bending models for thin shells. We first summarize existing bending models and then propose a new nonlinear, anisotropic bending model. In each subsection we state the surface energy per unit area and then define the stress and moment calculated using Eq. (20).

#### 3.1 Koiter bending model

The surface energy density for the Koiter bending model ([Ciarlet, 2005](#); [Steigmann, 2013](#)) is

$$W_{\text{bKo}} = \frac{1}{2} \mathbf{K} : \mathbb{F} : \mathbf{K}, \quad (45)$$

where the fourth order tensor  $\mathbb{F}$  is defined w.r.t.  $\mathbb{C}$  from Eq. (23) as

$$\mathbb{F} = \frac{T^2}{12} \mathbb{C}. \quad (46)$$

Here,  $T$  is the shell thickness. Inserting  $\mathbb{F}$  into Eq. (45) leads to

$$W_{\text{bKo}} = \frac{T^2}{24} \left( \Lambda (\text{tr} \mathbf{K})^2 + 2\mu K_{\alpha\beta} K^{\alpha\beta} \right), \quad (47)$$

where

$$\text{tr} \mathbf{K} = K^{\alpha\beta} A_{\alpha\beta}, \quad \text{and} \quad K^{\alpha\beta} := A^{\alpha\gamma} K_{\gamma\delta} A^{\delta\beta}, \quad (48)$$

similar to Eq. (24)-(25). According to Eq. (20), the Koiter bending model only causes the moment

$$M_{0 \text{bKo}}^{\alpha\beta} = \frac{T^2}{12} \left( \Lambda \text{tr} \mathbf{K} A^{\alpha\beta} + 2\mu K^{\alpha\beta} \right), \quad (49)$$

while  $\tau_{\text{bKo}}^{\alpha\beta} = 0$ . The surface Lamé parameters can be derived from Young's modulus ( $E$ ) and Poisson's ratio ( $\nu$ ) as ([Ciarlet, 2005](#))

$$\mu := \frac{TE}{2(1+\nu)}, \quad \Lambda := \frac{2\mu\nu}{1-\nu}, \quad (50)$$

that admit the special case  $\nu = 0.5$ . From these, one can identify the bending stiffness ([Landau and Lifshitz, 1986](#))

$$c_{\text{Koi}} = \frac{ET^3}{12(1-\nu^2)} = \frac{T^2}{12} (\Lambda + 2\mu). \quad (51)$$

### 3.2 Canham bending model

The surface energy density for the bending model of [Canham \(1970b\)](#) is of the form

$$W_{\text{Can}} = c J (2 H^2 - \kappa), \quad (52)$$

where  $c$  is the bending modulus with units [Nm]. According to Eq. (20), the Canham bending model contributes to both stress and moment as

$$\begin{aligned} \tau_{\text{Can}}^{\alpha\beta} &= c J (2 H^2 + \kappa) a^{\alpha\beta} - 4 c J H b^{\alpha\beta}, \\ M_{0\text{Can}}^{\alpha\beta} &= c J b^{\alpha\beta}. \end{aligned} \quad (53)$$

As seen,  $M_{0\text{Can}}^{\alpha\beta}$  is proportional to the total curvature  $b^{\alpha\beta}$  instead of the relative curvature  $K^{\alpha\beta}$  as for the Koiter model in Eq. (49). This makes the Canham model unsuitable for initially curved stress-free shells. Comparing their stiffness  $f^{\alpha\beta\gamma\delta}$ , further shows that the Canham and Koiter model are equivalent for small deformations of initially flat shells when

$$c = c_{\text{Can}} = \frac{\mu T^2}{6} \quad \text{and} \quad \Lambda = 0, \quad (54)$$

implying

$$c_{\text{Can}} = \frac{E T^3}{12} \quad (55)$$

according to Eq. (51).

### 3.3 Helfrich bending model

The surface energy density for the bending model of [Helfrich \(1973\)](#) is defined by

$$W_{\text{Hel}} = J (k (H - \bar{H}_0)^2 + \bar{k} \kappa), \quad (56)$$

where  $\bar{H}_0$  is the spontaneous curvature of the material, which can be an externally prescribed quantity, or taken as the initial mean curvature of the shell. Further,  $k$  and  $\bar{k}$  are material constants. The stress and moment follow from Eq. (20) as

$$\begin{aligned} \tau_{\text{Hel}}^{\alpha\beta} &= J (k \Delta H^2 - \bar{k} \kappa) a^{\alpha\beta} - 2 k J \Delta H b^{\alpha\beta}, \\ M_{0\text{Hel}}^{\alpha\beta} &= J (k \Delta H + 2 \bar{k} H) a^{\alpha\beta} - \bar{k} J b^{\alpha\beta}, \end{aligned} \quad (57)$$

with  $\Delta H := H - \bar{H}_0$ . This model reduces to the Canham model for  $\bar{H}_0 = 0$ ,  $k = 2c$ , and  $\bar{k} = -c$ . Comparing the stiffness  $f^{\alpha\beta\gamma\delta}$  ([Sauer and Duong, 2017](#)), shows that the Helfrich and Koiter bending model are equivalent in the linear regime if

$$k = \frac{T^2}{6} (\Lambda + 2\mu), \quad \text{and} \quad \bar{k} = -\frac{T^2 \mu}{6}, \quad (58)$$

which then implies  $c_{\text{Hel}} = c_{\text{Koi}}$ .

### 3.4 Analytically projected Neo-Hooke bending model (apH)

The classical 3D Neo-Hooke material model can be analytically integrated through the shell thickness as presented in [Duong et al. \(2017\)](#). Assuming incompressibility ( $\nu = 0.5$ ) this leads to the stress and moment ([Roohbakhshan and Sauer, 2017](#))

$$\begin{aligned}\tau_{\text{apH}}^{\alpha\beta} &= \mu \left( A^{\alpha\beta} - \frac{1}{J^2} a^{\alpha\beta} \right), \\ M_{0\text{apH}}^{\alpha\beta} &= -\frac{\mu T^2}{6} \left( B^{\alpha\beta} - \frac{1}{J^2} \left( b^{\alpha\beta} + 2(H - H_0) a^{\alpha\beta} \right) \right).\end{aligned}\quad (59)$$

Here,  $H_0$  refers to the mean curvature in the initial configuration. Model (59) becomes a pure membrane model if  $M_{0\text{apH}}^{\alpha\beta} = 0$ , i.e. for  $T^2 \rightarrow 0$ . Otherwise it is a complete shell model, meaning, it has both membrane and bending parts unlike the other models considered in this section. The bending moment parameter,  $c_{\text{apH}}$ , is the same as  $c_{\text{Koi}}$  in Eq. (51) as long as  $\nu = 0.5$ .

### 3.5 Proposed new bending model

The preceding bending models all have drawbacks, as will be shown in Sec. 4 and 5. This motivates the following new bending model defined by the surface energy density per reference area

$$W_{\text{new}} = \frac{c_1}{2} k_1^2 + \frac{c_2}{2} k_2^2 + c_{12} k_1 k_2 + \frac{c_3}{2} k_{12}^2, \quad (60)$$

where the kinematical quantities

$$k_i := \lambda_i \kappa_i - \kappa_{0i}, \quad i = 1, 2 \text{ (without summation)} \quad (61)$$

$$k_{12} := \sqrt{\lambda_1 \lambda_2} \kappa_{12} - \kappa_{012}, \quad (62)$$

characterize the relative curvature, and  $c_i$ ,  $c_{12}$  and  $c_3$  are bending moduli. The stretch ( $\lambda_i$ ) and curvature ( $\kappa_i$ ,  $\kappa_{0i}$ ,  $\kappa_{12}$  and  $\kappa_{012}$ ) measures are defined as (without summation on  $i$ )

$$\lambda_i := \sqrt{L_i^\alpha a_{\alpha\beta} L_i^\beta}, \quad (63)$$

$$\kappa_i := \frac{1}{\lambda_i^2} L_i^\alpha b_{\alpha\beta} L_i^\beta, \quad \kappa_{0i} := L_i^\alpha B_{\alpha\beta} L_i^\beta, \quad (64)$$

and

$$\kappa_{12} := \frac{L_1^\alpha L_2^\beta + L_2^\alpha L_1^\beta}{\lambda_1 \lambda_2} b_{\alpha\beta}, \quad \kappa_{012} := (L_1^\alpha L_2^\beta + L_2^\alpha L_1^\beta) B_{\alpha\beta}. \quad (65)$$

It is emphasized that these kinematic quantities do not depend on the choice of surface parameterization, hence making the new model frame invariant. Here  $\kappa_{0i}$ , for  $i = 1, 2$ , refers to the two principal surface curvatures in the initial configuration, while

$$L_i^\alpha = \mathbf{L}_i \cdot \mathbf{A}^\alpha \quad (66)$$

refers to the corresponding principal curvature directions in the initial configuration. As a consequence of Eqs. (63) and (64),  $\lambda_i$  and  $\kappa_i$  are generally not equal to the current principal stretches and curvatures. The proposed bending model is a generalization of the 1D fiber

bending model of Duong et al. (2020) that appears for  $c_2 = c_{12} = c_3 = 0$ . In contrast to the Canham model, the proposed bending model of Eq. (60) can be employed for initially stress-free curved shells.

The components of the membrane stress and bending moment follow from Eqs. (20) and (60) as

$$\begin{aligned}\tau_{\text{new}}^{\alpha\beta} &= - \left( c_1 k_1 + c_{12} k_2 + \frac{c_3 \sqrt{\lambda_2} \kappa_{12} k_{12}}{2 \sqrt{\lambda_1} \kappa_1} \right) \kappa_1 \ell_{11}^{\alpha\beta} \\ &\quad - \left( c_{12} k_1 + c_2 k_2 + \frac{c_3 \sqrt{\lambda_1} \kappa_{12} k_{12}}{2 \sqrt{\lambda_2} \kappa_2} \right) \kappa_2 \ell_{22}^{\alpha\beta}, \\ M_{0\text{new}}^{\alpha\beta} &= (c_1 k_1 + c_{12} k_2) \ell_{11}^{\alpha\beta} + (c_{12} k_1 + c_2 k_2) \ell_{22}^{\alpha\beta} + c_3 k_{12} \ell_{12}^{\alpha\beta},\end{aligned}\quad (67)$$

with

$$\ell_{11}^{\alpha\beta} := \frac{L_1^\alpha L_1^\beta}{\lambda_1}, \quad \ell_{22}^{\alpha\beta} := \frac{L_2^\alpha L_2^\beta}{\lambda_2}, \quad \ell_{12}^{\alpha\beta} := \frac{L_1^\alpha L_2^\beta + L_2^\alpha L_1^\beta}{\sqrt{\lambda_1 \lambda_2}}. \quad (68)$$

The fourth order material tangents and an efficient FE implementation for the new bending model are provided in Appendices A and B, respectively. Appendix C shows that for small deformations the proposed model is equivalent to the Koiter model, if

$$c_i = \frac{T^2}{12} (\Lambda + 2\mu), \quad c_{12} = \frac{T^2}{12} \Lambda, \quad \text{and} \quad c_3 = \frac{T^2}{12} \mu. \quad (69)$$

$c_1$  and  $c_2$  then play the same role as  $c_{\text{Koi}}$ .

**Remark 3.1:** The Canham bending model is a special case of the proposed new model when  $\kappa_{0i} = 0$ ,  $\lambda_i = \sqrt{J}$ ,  $c_i = c$  and  $c_{12} = c_3 = 0$ .

## 4 Elementary bending test cases

In this section, three analytical test cases are investigated, and the results for the proposed new bending material model are juxtaposed with the results for the other bending models given in the previous section. In all the test cases considered, the initial configuration of a tube with radius  $R$  and length  $L = \pi R$  is considered. The initial surface of the tube can be parametrized using

$$\theta \in [-\pi/2, \pi/2] \text{ and } \phi \in [0, \pi], \quad (70)$$

to represent any point on it as

$$\mathbf{X}(\theta, \phi) = R \mathbf{e}_r + R \phi \mathbf{e}_3, \quad (71)$$

with

$$\mathbf{e}_r = \cos \theta \mathbf{e}_1 + \sin \theta \mathbf{e}_2, \quad (72)$$

$$\mathbf{e}_\theta = -\sin \theta \mathbf{e}_1 + \cos \theta \mathbf{e}_2. \quad (73)$$

The tangents and normal for this surface then follow from (3) as

$$\mathbf{A}_1 = \frac{\partial \mathbf{X}}{\partial \theta} = R \mathbf{e}_\theta, \quad (74)$$

$$\mathbf{A}_2 = \frac{\partial \mathbf{X}}{\partial \phi} = R \mathbf{e}_3, \quad (75)$$

and

$$\mathbf{N} = \frac{\mathbf{A}_1 \times \mathbf{A}_2}{\|\mathbf{A}_1 \times \mathbf{A}_2\|} = \mathbf{e}_r. \quad (76)$$

Using these, we can obtain the further quantities

$$[A_{\alpha\beta}] = R^2 \begin{bmatrix} 1 & 0 \\ 0 & 1 \end{bmatrix}, \quad [A^{\alpha\beta}] = \frac{1}{R^2} \begin{bmatrix} 1 & 0 \\ 0 & 1 \end{bmatrix}, \quad (77)$$

$$[B_{\alpha\beta}] = -R \begin{bmatrix} 1 & 0 \\ 0 & 0 \end{bmatrix}, \quad [B_{\beta}^{\alpha}] = -\frac{1}{R} \begin{bmatrix} 1 & 0 \\ 0 & 0 \end{bmatrix}, \quad [B^{\alpha\beta}] = -\frac{1}{R^3} \begin{bmatrix} 1 & 0 \\ 0 & 0 \end{bmatrix}, \quad (78)$$

$$\mathbf{L}_1 = \mathbf{e}_{\theta}, \quad \mathbf{L}_2 = \mathbf{e}_3, \quad (79)$$

$$L_1^1 = \frac{1}{R}, \quad L_1^2 = 0, \quad L_2^1 = 0, \quad L_2^2 = \frac{1}{R}, \quad (80)$$

and

$$\kappa_{01} = -\frac{1}{R}, \quad \kappa_{02} = 0. \quad (81)$$

In the elementary test cases that follow, we use  $\Lambda = 0$  and  $\mu T^2/6 = c$  for all the models except the proposed new model. For the new bending model, the bending parameters are considered to be arbitrary and  $c_1 = c_2 = c$ . This generalization is used so that all the bending models can be compared with the proposed model through a common material parameter. Further, for the Helfrich model, the corresponding material constants are taken from Eq. (58) and the spontaneous curvature is set to the initial mean curvature value  $\bar{H}_0 = -1/(2R)$ .

## 4.1 Test case 1 – bending vs. rigid rotation

As shown in Fig. 1, the first test case compares the stresses and moments for two similarly looking but differently obtained final configurations. One is obtained by applying a rigid body rotation and thus no stress or moment should be induced. The other is obtained by counter bending, wherein stress and moment are induced. This test examines whether the principal curvatures are assigned properly during deformation. This is essential for bending models directly defined on the principal curvatures, such as our proposed model.

### 4.1.1 Rigid body rotation

Given the parametrization of Eq. (70), the current configuration of the half tube rotated by  $90^\circ$  around the  $\mathbf{e}_2$ -axis (Fig. 1a) is described by

$$\mathbf{x} = R \cos \theta \mathbf{e}_1 + R \phi \mathbf{e}_2 - R \sin \theta \mathbf{e}_3. \quad (82)$$

The tangents, normal, surface metric and curvature tensor components thus are

$$\mathbf{a}_1 = -R \sin \theta \mathbf{e}_1 - R \cos \theta \mathbf{e}_3, \quad \mathbf{a}_2 = R \mathbf{e}_2, \quad \mathbf{n} = \cos \theta \mathbf{e}_1 - \sin \theta \mathbf{e}_3, \quad (83)$$

and

$$[a_{\alpha\beta}] = R^2 \begin{bmatrix} 1 & 0 \\ 0 & 1 \end{bmatrix} = [A_{\alpha\beta}], \quad [b_{\alpha\beta}] = -R \begin{bmatrix} 1 & 0 \\ 0 & 0 \end{bmatrix} = [B_{\alpha\beta}]. \quad (84)$$

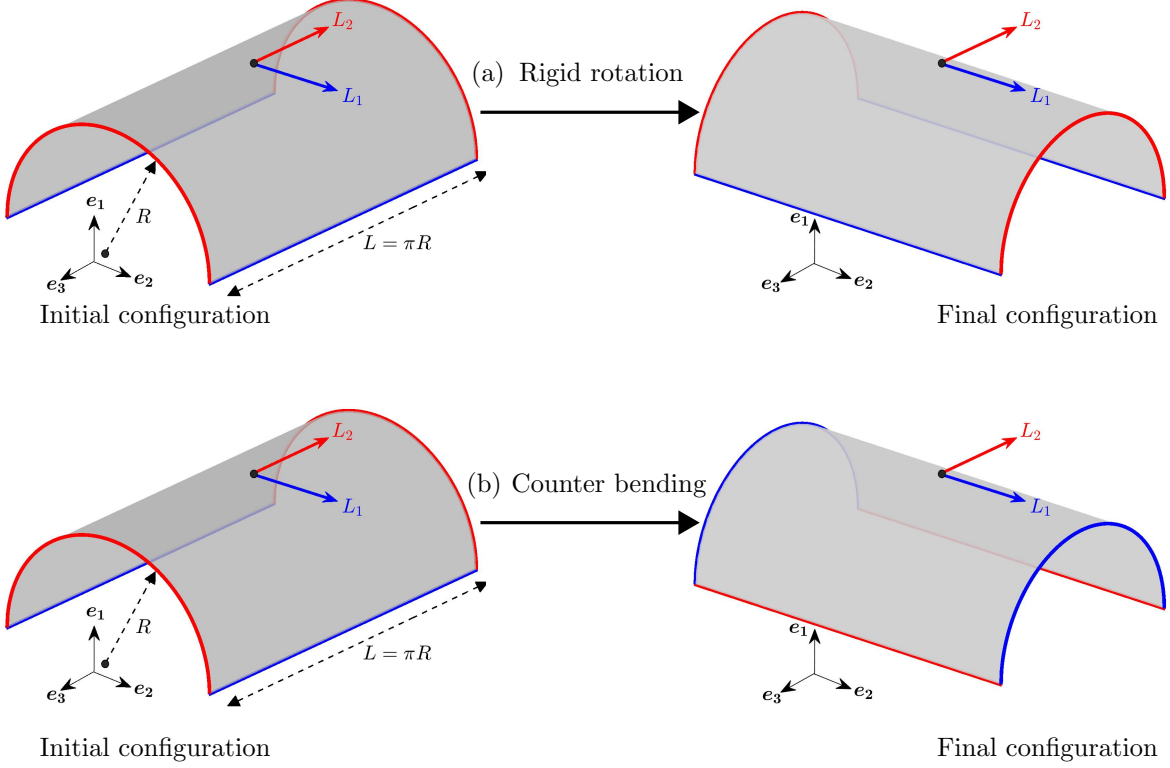


**Figure 1:** Test case 1: Initial and final configuration for (a) rigid body rotation and (b) counter bending.

	$\tau_{\beta}^{\alpha}$	$M_{\beta 0}^{\alpha}$	$N_{\beta}^{\alpha}$
Koiter	0	0	0
Canham	$\frac{c \kappa_1^2}{2} \begin{bmatrix} -3 & 0 \\ 0 & 1 \end{bmatrix}$	$c \kappa_1 \begin{bmatrix} 1 & 0 \\ 0 & 0 \end{bmatrix}$	$\frac{c \kappa_1^2}{2} \begin{bmatrix} -1 & 0 \\ 0 & 1 \end{bmatrix}$
Helfrich	0	$c \kappa_1 \begin{bmatrix} 0 & 0 \\ 0 & -1 \end{bmatrix}$	0
apH	0	0	0
new	0	0	0

**Table 2:** Stress components for test case 1(a) – rigid body rotation – according to various bending models. For initially stress-free shells, all stresses should be zero in this test case, which is only satisfied by the Koiter, apH and new model.

As the body is not deforming, i.e.  $a_{\alpha\beta} = A_{\alpha\beta}$  and  $b_{\alpha\beta} = B_{\alpha\beta}$ , there should be no stress or bending moment induced. This can be verified by plugging the current stretch and curvature

along the principal curvature directions,

$$H = -\frac{1}{2R}, \quad \kappa = 0, \quad (85)$$

$$\lambda_1 = \lambda_2 = 1, \quad (86)$$

$$\kappa_1 = -\frac{1}{R} = \kappa_{01}, \quad \kappa_2 = 0, \quad (87)$$

into the equations of Sec. 3. The results are enumerated in Table 2. As seen, for the Koiter, apH and proposed new model no stress or moment are introduced. However, for the Canham model we obtain both non-zero stress and moment and for the Helfrich model, a non-zero moment. This is because for the considered initial configuration, these two models are not completely stress-free. The Helfrich bending model only satisfies this test for  $\bar{k} = 0$  as otherwise the bending stress  $M_{0\text{Hel}}^{\alpha\beta}$  becomes non-zero even when  $\Delta H = 0$  as seen in Eq. (57.2).

#### 4.1.2 Counter bending

A similarly looking final configuration as before can be obtained by the counter bending shown in Fig. 1b. In this case the current configuration is given by

$$\mathbf{x} = R \sin \phi \mathbf{e}_1 - R \theta \mathbf{e}_2 + R \cos \phi \mathbf{e}_3. \quad (88)$$

The required kinematic quantities then are

$$\mathbf{a}_1 = -R \mathbf{e}_2, \quad \mathbf{a}_2 = R \cos \phi \mathbf{e}_1 - R \sin \phi \mathbf{e}_3, \quad \mathbf{n} = \sin \phi \mathbf{e}_1 + \cos \phi \mathbf{e}_3, \quad (89)$$

$$[a_{\alpha\beta}] = R^2 \begin{bmatrix} 1 & 0 \\ 0 & 1 \end{bmatrix} = [A_{\alpha\beta}], \quad (90)$$

$$[b_{\alpha\beta}] = -R \begin{bmatrix} 0 & 0 \\ 0 & 1 \end{bmatrix}, \quad [b_{\beta}^{\alpha}] = -\frac{1}{R} \begin{bmatrix} 0 & 0 \\ 0 & 1 \end{bmatrix}, \quad [b^{\alpha\beta}] = -\frac{1}{R^3} \begin{bmatrix} 0 & 0 \\ 0 & 1 \end{bmatrix}, \quad (91)$$

$$H = -\frac{1}{2R}, \quad \kappa = 0, \quad (92)$$

$$\lambda_1 = \lambda_2 = 1, \quad (93)$$

and

$$\kappa_1 = 0, \quad \kappa_2 = -\frac{1}{R} = \kappa_{01}. \quad (94)$$

Unlike the rigid body rotation considered before, the bending described by Eq. (88) generates non-zero bending moment components. Given the nature of the final configuration in this test case, the bending moment induced here should satisfy  $M_1^1 = -M_2^2$ , while the Cauchy stress components,  $N_{\beta}^{\alpha}$ , should still be zero. The stress and moment components of the five bending models are shown in Tab. 3. The Canham model neither provides accurate bending moment nor Cauchy stress components. While the Helfrich model gives accurate Cauchy stress and erroneous bending moment, the apH and Koiter models give accurate bending moments but not Cauchy stresses. Only if  $\kappa_2$  is small (corresponding to small deformations)  $\kappa_2^2$  becomes negligible, and hence satisfactory Cauchy stresses are obtained. Thus the Koiter and apH model can be argued to partially pass the test. But only the new model fully passes the test. The test also illustrates its anisotropic nature: If the bending parameter  $c_1 \neq c_2$  then  $M_1^1/(c_1 - c_{12}) = -M_2^2/(c_2 - c_{12})$ .

	$\tau_\beta^\alpha$	$M_{\beta 0}^\alpha$	$N_\beta^\alpha$
Koiter	0	$c \kappa_2 \begin{bmatrix} -1 & 0 \\ 0 & 1 \end{bmatrix}$	$c \kappa_2^2 \begin{bmatrix} 0 & 0 \\ 0 & 1 \end{bmatrix}$
Canham	$\frac{c \kappa_2^2}{2} \begin{bmatrix} 1 & 0 \\ 0 & -3 \end{bmatrix}$	$c \kappa_2 \begin{bmatrix} 0 & 0 \\ 0 & 1 \end{bmatrix}$	$\frac{c \kappa_2^2}{2} \begin{bmatrix} 1 & 0 \\ 0 & -1 \end{bmatrix}$
Helfrich	0	$c \kappa_2 \begin{bmatrix} -1 & 0 \\ 0 & 0 \end{bmatrix}$	0
apH	0	$c \kappa_2 \begin{bmatrix} -1 & 0 \\ 0 & 1 \end{bmatrix}$	$c \kappa_2^2 \begin{bmatrix} 0 & 0 \\ 0 & 1 \end{bmatrix}$
new	$(c_{12} - c) \kappa_2^2 \begin{bmatrix} 0 & 0 \\ 0 & 1 \end{bmatrix}$	$(c - c_{12}) \kappa_2 \begin{bmatrix} -1 & 0 \\ 0 & 1 \end{bmatrix}$	0

**Table 3:** Stress components for test case 1(b) – counter bending – according to various bending models. In this case, the Cauchy stress  $N_\beta^\alpha$  should be zero while  $M_1^1$  should be equal to  $-M_2^2$ , which is only satisfied by the new model.

## 4.2 Test case 2 – bending vs. stretching

Test case 2 also examines the behavior of two similarly looking yet different deformations. They are now obtained either by inflation or bending, as Fig. 2 shows.

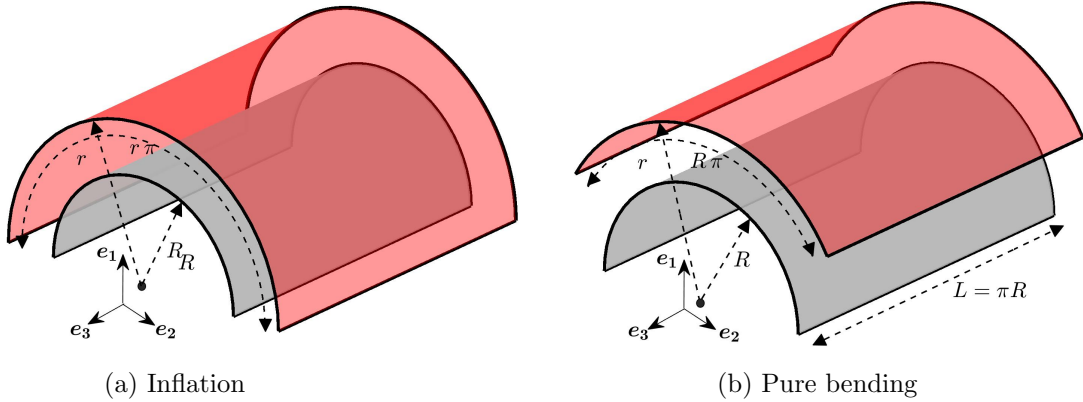


**Figure 2:** Test case 2: initial (grey) and final (red) configurations for (a) inflation and (b) pure bending.

### 4.2.1 Inflation

If the half tube is inflated to have radius  $r$  (Fig. 2a), the current configuration is given by

$$\mathbf{x} = r \mathbf{e}_r + R \phi \mathbf{e}_3, \quad (95)$$

based on Eqs. (70) and (72). While the components of the curvature tensor are the same as in Eq. (78), but with  $R$  replaced by  $r$ , the surface metric now is

$$[a_{\alpha\beta}] = \begin{bmatrix} r^2 & 0 \\ 0 & R^2 \end{bmatrix}. \quad (96)$$

The stretch and curvature terms are then of the form

$$H = -\frac{1}{2r}, \quad \kappa = 0, \quad (97)$$

$$\lambda_1 = \frac{r}{R}, \quad \lambda_2 = 1, \quad (98)$$

and

$$\kappa_1 = -\frac{1}{r}, \quad \kappa_2 = 0. \quad (99)$$

The resulting stress and moment components for test case 2(a) are listed in Tab. 4. The deformation considered here is a pure membrane action, and hence any stress contribution should only stem from the membrane part but not from the bending part of the material model. This is achieved by our new bending model as it does not introduce any stress or bending moment even though the surface curvature changes. Also the apH model achieves this for  $\tau^{\alpha\beta}$  (which comes from the membrane stiffness  $\mu$ ), but not for  $M_\beta^\alpha$  and  $N_\beta^\alpha$  (which are affected by bending stiffness  $c$ ). All other models show unphysical stresses in all components. In case of the Koiter and apH model, those vanish in the limit  $r \rightarrow R$ , i.e., for small  $\Delta\kappa_1 := \kappa_1 - \kappa_{01}$ . In case of the Canham and Helfrich bending models non-zero stresses remain even for small  $\Delta\kappa_1$ .

	$\tau_\beta^\alpha$	$M_{\beta 0}^\alpha$	$N_\beta^\alpha$
Koiter	0	$c\Delta\kappa_1 \frac{\kappa_{01}^3}{\kappa_1^3} \begin{bmatrix} -1 & 0 \\ 0 & 0 \end{bmatrix}$	$c\Delta\kappa_1 \frac{\kappa_{01}^2}{\kappa_1} \begin{bmatrix} 1 & 0 \\ 0 & 0 \end{bmatrix}$
Canham	$\frac{cJ\kappa_1^2}{2} \begin{bmatrix} -3 & 0 \\ 0 & 1 \end{bmatrix}$	$cJ\kappa_1 \begin{bmatrix} 1 & 0 \\ 0 & 0 \end{bmatrix}$	$\frac{c\kappa_1^2}{2} \begin{bmatrix} -1 & 0 \\ 0 & 1 \end{bmatrix}$
Helfrich	$\frac{-Jc\Delta\kappa_1}{2} \begin{bmatrix} \kappa_{01} + 3\kappa_1 & 0 \\ 0 & -\Delta\kappa_1 \end{bmatrix}$	$Jc \begin{bmatrix} \Delta\kappa_1 & 0 \\ 0 & -\kappa_{01} \end{bmatrix}$	$\frac{-c\Delta\kappa_1}{2} \begin{bmatrix} \kappa_{01} + \kappa_1 & 0 \\ 0 & -\Delta\kappa_1 \end{bmatrix}$
apH	$\frac{-\mu\Delta\kappa_1}{\kappa_{01}^2} \begin{bmatrix} \frac{e}{\kappa_1^2} & 0 \\ 0 & \kappa_{01} + \kappa_1 \end{bmatrix}$ with $e := (\kappa_{01} + \kappa_1)(\kappa_{01}^2 + \kappa_1^2)$	$\frac{c\Delta\kappa_1}{\kappa_{01}^2} \begin{bmatrix} \frac{d}{\kappa_1^2} & 0 \\ 0 & \kappa_1^2 \end{bmatrix}$ with $d := 2\kappa_1^4 + \kappa_{01}e$	$\frac{-\Delta\kappa_1}{\kappa_{01}^3\kappa_1} \begin{bmatrix} \mu e - cd\kappa_1 & 0 \\ 0 & \mu\kappa_1^2(\kappa_{01} + \kappa_1) \end{bmatrix}$
new	0	0	0

**Table 4:** Stress components for test case 2(a) – inflation – according to various bending models. In this case, all bending induced stresses ( $\tau_\beta^\alpha$ ,  $M_\beta^\alpha$  and  $N_\beta^\alpha$ ) should be zero, which is only achieved by the new bending model.  $\Delta\kappa_1 := \kappa_1 - \kappa_{01}$  is introduced for simplification.

#### 4.2.2 Pure bending

In the second case, the half tube undergoes pure bending to have the radius  $r$  and length  $l$  without any change in the arc length (Fig. 2b). The current configuration, parametrized by Eq. (70), is now described by

$$\mathbf{x} = r \mathbf{e}_{\tilde{r}} + R \phi \mathbf{e}_3, \quad (100)$$

where

$$\mathbf{e}_{\tilde{r}} := \cos\left(\frac{R\theta}{r}\right) \mathbf{e}_1 + \sin\left(\frac{R\theta}{r}\right) \mathbf{e}_2, \quad (101)$$

$$\mathbf{e}_{\tilde{\theta}} := -\sin\left(\frac{R\theta}{r}\right) \mathbf{e}_1 + \cos\left(\frac{R\theta}{r}\right) \mathbf{e}_2. \quad (102)$$

The corresponding tangents and normal vectors then follow as

$$\mathbf{a}_1 = R \mathbf{e}_{\tilde{\theta}}, \quad \mathbf{a}_2 = R \mathbf{e}_3, \quad \mathbf{N} = \mathbf{e}_{\tilde{r}}. \quad (103)$$

Further, the surface metric and curvature tensor components become

$$[a_{\alpha\beta}] = R^2 \begin{bmatrix} 1 & 0 \\ 0 & 1 \end{bmatrix} = [A_{\alpha\beta}], \quad (104)$$

$$[b_{\alpha\beta}] = -\frac{R^2}{r} \begin{bmatrix} 1 & 0 \\ 0 & 0 \end{bmatrix}, \quad [b_{\beta}^{\alpha}] = -\frac{1}{r} \begin{bmatrix} 1 & 0 \\ 0 & 0 \end{bmatrix}, \quad [b^{\alpha\beta}] = -\frac{1}{rR^2} \begin{bmatrix} 1 & 0 \\ 0 & 0 \end{bmatrix}. \quad (105)$$

With this the stretch and curvature can be calculated as

$$H = -\frac{1}{2r}, \quad \kappa = 0, \quad (106)$$

$$\lambda_1 = \lambda_2 = 1, \quad (107)$$

and

$$\kappa_1 = -\frac{1}{r}, \quad \kappa_2 = 0. \quad (108)$$

The resulting stress and moment components for test case 2(b) are listed in Tab. 5. The components of Cauchy stress  $N_{\beta}^{\alpha}$  should be zero, and only our new bending model accurately captures this.

	$\tau_{\beta}^{\alpha}$	$M_{\beta 0}^{\alpha}$	$N_{\beta}^{\alpha}$
Koiter	0	$c \Delta \kappa_1 \begin{bmatrix} 1 & 0 \\ 0 & 0 \end{bmatrix}$	$c \Delta \kappa_1 \kappa_1 \begin{bmatrix} 1 & 0 \\ 0 & 0 \end{bmatrix}$
Canham	$\frac{c \kappa_1^2}{2} \begin{bmatrix} -3 & 0 \\ 0 & 1 \end{bmatrix}$	$c \kappa_1 \begin{bmatrix} 1 & 0 \\ 0 & 0 \end{bmatrix}$	$\frac{c \kappa_1^2}{2} \begin{bmatrix} -1 & 0 \\ 0 & 1 \end{bmatrix}$
Helfrich	$\frac{-c \Delta \kappa_1}{2} \begin{bmatrix} 3 \kappa_1 + \kappa_{01} & 0 \\ 0 & -\Delta \kappa_1 \end{bmatrix}$	$c \begin{bmatrix} \Delta \kappa_1 & 0 \\ 0 & -\kappa_{01} \end{bmatrix}$	$\frac{-c \Delta \kappa_1}{2} \begin{bmatrix} \kappa_{01} + \kappa_1 & 0 \\ 0 & -\Delta \kappa_1 \end{bmatrix}$
apH	0	$c \Delta \kappa_1 \begin{bmatrix} 2 & 0 \\ 0 & 1 \end{bmatrix}$	$2 c \kappa_1 \Delta \kappa_1 \begin{bmatrix} 1 & 0 \\ 0 & 0 \end{bmatrix}$
new	$-c \Delta \kappa_1 \kappa_1 \begin{bmatrix} 1 & 0 \\ 0 & 0 \end{bmatrix}$	$\Delta \kappa_1 \begin{bmatrix} c & 0 \\ 0 & c_{12} \end{bmatrix}$	0

**Table 5:** Stress components for test case 2(b) – pure bending – according to various bending models.  $N_{\beta}^{\alpha}$  should be zero in this case, which is only achieved by the new model.  $\Delta \kappa_1 := \kappa_1 - \kappa_{01}$  is introduced to simplify the results.

### 4.3 Test case 3 - Torsion

Unlike in the previous test cases, we now consider an open ended full cylinder and parametrize it using

$$\theta \in [0, 2\pi], \text{ and } \phi \in [0, \pi]. \quad (109)$$

The initial surface, shown in Fig. 3a, can still be described using Eq. (71). Twisting is then described by (see Fig. 3b)

$$\mathbf{x}(\theta, \phi) = R \mathbf{e}_{\bar{r}} + R \phi \mathbf{e}_3, \quad (110)$$

where

$$\mathbf{e}_{\bar{r}} := \cos(\theta + \gamma\phi) \mathbf{e}_1 + \sin(\theta + \gamma\phi) \mathbf{e}_2, \quad (111)$$

$$\mathbf{e}_{\bar{\theta}} := -\sin(\theta + \gamma\phi) \mathbf{e}_1 + \cos(\theta + \gamma\phi) \mathbf{e}_2. \quad (112)$$

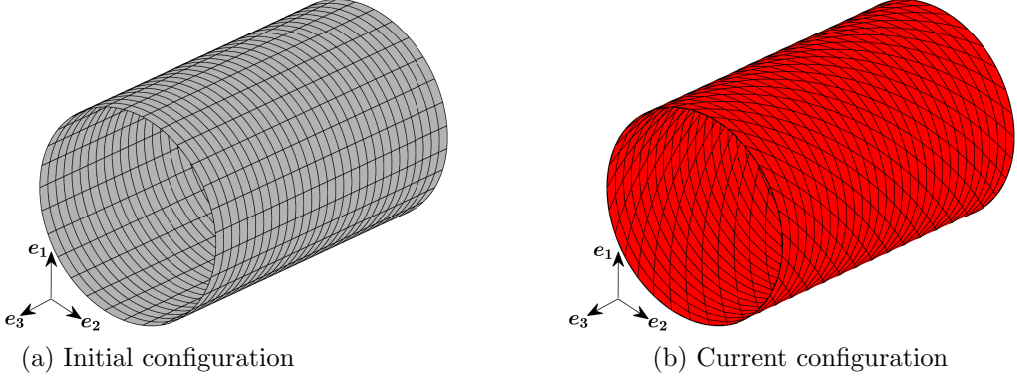


**Figure 3:** Torsion: Initial and final configuration.

Here  $\gamma$  is a constant that defines the extent of twisting. The tangent vectors and normal follow from Eq. (10) as

$$\mathbf{a}_1 = R \mathbf{e}_{\bar{\theta}}, \quad (113)$$

$$\mathbf{a}_2 = R (\mathbf{e}_{\bar{\theta}} + \mathbf{e}_3), \quad (114)$$

$$\mathbf{n} = \mathbf{e}_{\bar{r}}, \quad (115)$$

while the kinematic quantities become

$$[a_{\alpha\beta}] = R^2 \begin{bmatrix} 1 & \gamma \\ \gamma & (\gamma^2 + 1) \end{bmatrix}, \quad [a^{\alpha\beta}] = \frac{1}{R^2} \begin{bmatrix} (\gamma^2 + 1) & -\gamma \\ -\gamma & 1 \end{bmatrix}, \quad (116)$$

$$[b_{\alpha\beta}] = -R \begin{bmatrix} 1 & \gamma \\ \gamma & \gamma^2 \end{bmatrix}, \quad [b_{\beta}^{\alpha}] = -\frac{1}{R} \begin{bmatrix} 1 & \gamma \\ 0 & 0 \end{bmatrix}, \quad [b^{\alpha\beta}] = -\frac{1}{R^3} \begin{bmatrix} 1 & 0 \\ 0 & 0 \end{bmatrix}, \quad (117)$$

$$H = -\frac{1}{2R}, \quad \kappa = 0, \quad (118)$$

$$\lambda_1 = 1, \quad \lambda_2 = \sqrt{\gamma^2 + 1}, \quad (119)$$

and

$$\kappa_1 = -\frac{1}{R}, \quad \kappa_2 = -\frac{\gamma^2}{R(\gamma^2 + 1)}. \quad (120)$$

We emphasize that the principal curvatures in the current configuration,  $\kappa_i^*$ , which follow from Eq. (8) as

$$\kappa_1^* = -\frac{1}{R}, \quad \kappa_2^* = 0, \quad (121)$$

will be different from  $\kappa_i$ .

	$\tau^{\alpha\beta}$	$M_0^{\alpha\beta}$	$N_\beta^\alpha$
Koiter	0	$c\kappa_1^3 \begin{bmatrix} 0 & \gamma \\ \gamma & \gamma^2 \end{bmatrix}$	$c\kappa_1^2\gamma \begin{bmatrix} \gamma & \gamma^2 \\ \lambda_2^2 & \lambda_2\gamma_2 \end{bmatrix}$
Canham	$\frac{c\kappa_1^4}{2} \begin{bmatrix} \gamma^2 - 3 & -\gamma \\ \gamma & 1 \end{bmatrix}$	$c\kappa_1^3 \begin{bmatrix} 1 & 0 \\ 0 & 0 \end{bmatrix}$	$\frac{c\kappa_1^2}{2} \begin{bmatrix} -1 & -2\gamma \\ 0 & 1 \end{bmatrix}$
Helfrich	0	$c\kappa_1^3 \begin{bmatrix} -\gamma^2 & \gamma \\ \gamma & -1 \end{bmatrix}$	0
apH	$\mu\kappa_1^2 \begin{bmatrix} -\gamma^2 & \gamma \\ \gamma & 0 \end{bmatrix}$	0	$\mu \begin{bmatrix} 0 & \gamma \\ \gamma & \gamma^2 \end{bmatrix}$
new	$-\frac{\gamma^2\kappa_1^4}{\lambda_2} \begin{bmatrix} c_{12} + 2c_3 & 0 \\ 0 & \frac{c\gamma^2}{\lambda_2^3} + \frac{2c_3}{\lambda_2^2} \end{bmatrix}$	$\frac{\gamma\kappa_1^3}{\lambda_2} \begin{bmatrix} c_{12}\gamma & 2c_3 \\ 2c_3 & \frac{c\gamma}{\lambda_2} \end{bmatrix}$	$\frac{\gamma\kappa_1^2}{\lambda_2^4} \begin{bmatrix} 0 & 0 \\ c\gamma^2 + 2c_3\lambda_2 & 0 \end{bmatrix}$

**Table 6:** Stress components for test case 3 – torsion. This test case should satisfy  $M_0^{11} = 0$  and  $M_0^{22} \neq 0$ , which is only achieved by the Koiter and the proposed new model (when  $c_{12} = 0$ ). The undesired membrane stress contributions from all bending models are much smaller than the stress contributions from a membrane model, even at large deformation.

From the Fig. 3, we know that  $M_0^{22}$  should be non-zero, as the fibers along  $\xi^2 = \phi$  are being bent. In contrast,  $M_0^{11}$  should be equal to zero, as there is no change in curvature of the fibers along  $\xi^1 = \theta$ . As shown in Tab. 6, only the Koiter model has  $M_0^{11} = 0$  and  $M_0^{22} \neq 0$ . For the proposed new model,  $M_0^{22} \neq 0$  and if we consider  $\Lambda = 0$ , which is also used for all the other bending models,  $M_0^{11}$  will be zero according to Eq. (69).

As torsion, in contrast to the previous test cases, causes in-plane deformation, we need to compare any stresses coming from the bending model to those of the membrane part of the material model in order to further asses the accuracy of the model. For this, we consider the Neo-Hookean membrane model defined in Eq. (27). Using Eq. (28), the Neo-Hookean's stress contribution will be

$$[\tau_{\text{mNH}}^{\alpha\beta}] = \mu\kappa_1^2 \begin{bmatrix} -\gamma^2 & \gamma \\ \gamma & 0 \end{bmatrix}. \quad (122)$$

Let  $\Lambda = 0$ ,  $\gamma = 1$  and slenderness ratio  $R/T = 100$ . Then, using Eq. (69), (122) and  $\tau_{\text{new}}^{\alpha\beta}$  in Tab. 6, the maximum absolute value of the effective membrane stress component of the new bending model ( $\tau_{\text{new}}^{11}$ ) and the Neo-Hookean membrane model ( $\tau_{\text{mNH}}^{11}$ ) can be compared. We find

$$\tau_{\text{new}}^{\alpha\beta \text{ max}} = 10^{-5} \frac{\mu}{R^2} \ll \tau_{\text{mNH}}^{\alpha\beta \text{ max}} = \frac{\mu}{R^2}. \quad (123)$$

The membrane stress contribution coming from the new material model is thus negligible ( $10^5$  times smaller) in comparison to the stress from the Neo-Hookean membrane model. The Eq. (123) also holds true for the new bending model's Cauchy stress  $N_{\text{new}}^{\alpha\beta}$ . The Canham bending model's membrane and Cauchy stress contributions are also of the same order as the new model, as Tab. 6 shows. The stress contribution from the apH model is equal to Eq. (122), which is acceptable as it is from its membrane part Eq. (59.1). Additionally, the Cauchy stress of the Koiter bending model ( $N_{\text{bKo}}^{\alpha\beta}$ ) will also be  $10^5$  times smaller than the Cauchy stress of the Koiter membrane model ( $N_{\text{mKo}}^{\alpha\beta} = \tau_{\text{mKo}}^{\alpha\beta}$ ) according to Eq. (26).

#### 4.4 Summary

The preceding results are categorized as passing, failing, or partial passing depending on the results of  $M_\beta^\alpha$  and  $N_\beta^\alpha$ . This categorization is shown in Tab. 7. As seen, only the proposed new bending model passes all test cases. In the table, an additional row is added to report if the models allow for initially stress-free curved surfaces. This is not the case for the Canham and Helfrich model. As a result of not being initially stress-free, the Canham and Helfrich models also fail to provide satisfying results for  $M_\beta^\alpha$  or  $N_\beta^\alpha$  in any of the elementary test cases where the body undergoes large deformation. The Koiter and apH models perform similarly well for all the test cases apart from torsion. Both the models pass test case 1(a), but only pass test case 1(b), when  $\kappa_2$  is small, such that errors in  $N_\beta^\alpha$  become negligible. They also only pass test case 2(a), when  $\Delta\kappa_1$  is negligible, due to errors in  $M_\beta^\alpha$ . In test case 2(b), the Koiter and apH models fail due to errors in both  $M_\beta^\alpha$  and  $N_\beta^\alpha$ . Test case 3 is passed by the Koiter, but not the apH model due to incorrect bending moments.

		Koiter	Canham	Helfrich	apH	new
0	initially stress-free	✓	✗	✗	✓	✓
1	a. rigid body rotation	✓	✓	✓	✓	✓
	b. counter bending	[✓]	✗	✗	[✓]	✓
2	a. inflation	{✓}	✗	✗	{✓}	✓
	b. pure bending	✗	✗	✗	✗	✓
3	torsion	✓	✗	✗	✗	✓

**Table 7:** Results of the elementary bending test cases:  $\text{✗}$  = test failed for either  $M_\beta^\alpha$  or  $N_\beta^\alpha$ ,  $\checkmark$  = test passed for both  $M_\beta^\alpha$  and  $N_\beta^\alpha$ ,  $[\checkmark]$  = test passed for  $M_\beta^\alpha$  but with errors in  $N_\beta^\alpha$  and  $\{\checkmark\}$  = test passed for  $N_\beta^\alpha$  but with errors in  $M_\beta^\alpha$ . Only the proposed new bending model passes all test cases.

## 5 Numerical examples

In this section, the performance of the new bending model is illustrated through two linear and three nonlinear numerical examples. In all examples, unless mentioned otherwise, the in-plane behavior is always modeled by the Koiter membrane model of Eq. (22), while the out-of-plane behavior is modeled by the different bending models of Sec. 3, which are then compared. The two linear examples demonstrate that the new bending model is equivalent to existing models in the small deformation regime. The three nonlinear examples illustrate that major differences appear at large deformations.

## 5.1 Simply supported plate under pressure loading

A simply supported square plate of length  $L = 12L_0$  and thickness  $T = 0.375L_0$  under the sinusoidal pressure

$$p(x, y) = \sin\left(\frac{\pi x}{L}\right) \sin\left(\frac{\pi y}{L}\right) E_0, \quad (124)$$

is analysed. The plate is considered to have Young's Modulus  $E = 480E_0$  and Poisson's ratio  $\nu = 0.38$ . Tab. 8 shows the list of corresponding parameters for the different bending models. As the problem is symmetric, only 1/4 of the plate is modeled and the symmetry boundary conditions are enforced using the penalty method of Duong et al. (2017) with penalty parameter  $\epsilon = 4.8n^{q-1}E_0L_0$ . Here,  $n$  refers to the number of elements per side and  $q$  is the order of shape functions used.

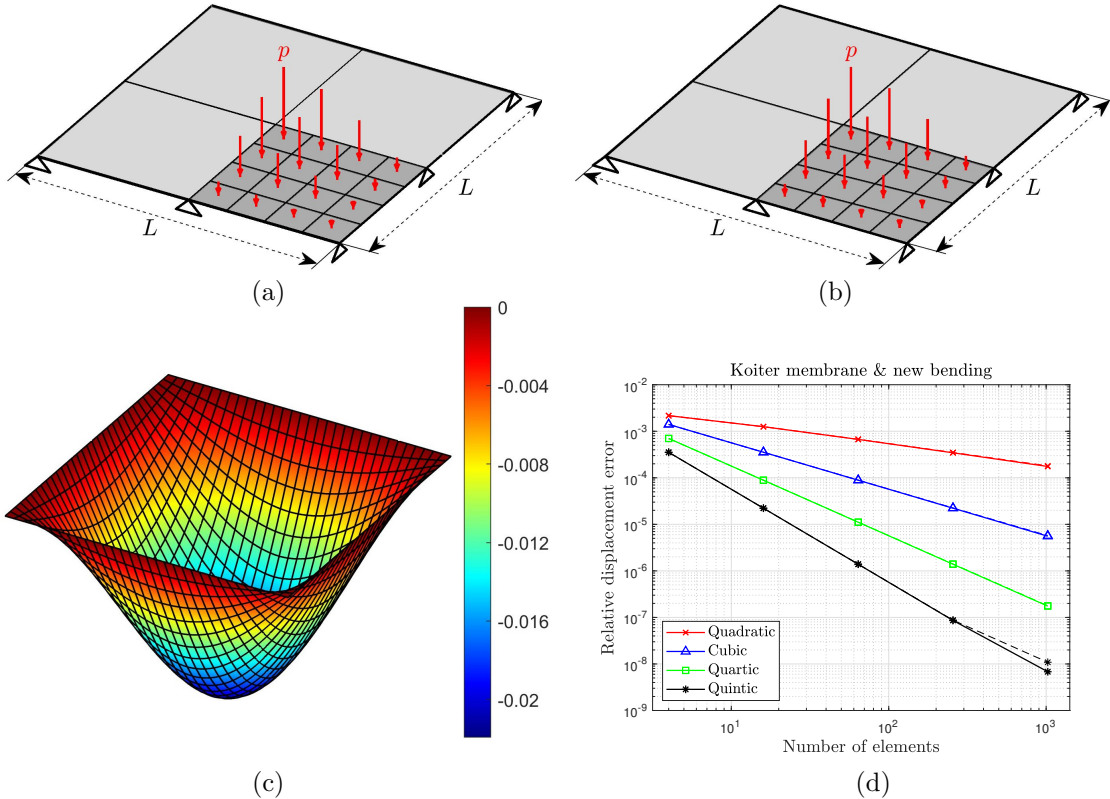


**Figure 4:** Simply supported plate: Problem setup with (a) regular mesh and (b) skewed mesh. (c) Deformed configuration (scaled by 400) for the skewed mesh colored by the vertical displacement. (d) Difference of the center displacement between analytical and numerical solution for the new bending model. The solid lines show the results of the regular mesh, while the dashed lines are the results of the skewed mesh. The displacements obtained for the other bending models are similar to the new bending model and hence omitted here.

The maximum vertical displacement is compared to the analytical solution from Ugural (2009) and the relative error plot is shown in Fig. 4d for the new bending model. All the other bending models show matching error rates and are therefore omitted from the error plot. In this plot, the results obtained with a regular mesh (Fig. 4a) and skewed mesh (Fig. 4b) are compared using solid and dashed lines, respectively. The two results are very close, confirming that the new bending model works also when  $\mathbf{L}_i$  is not aligned with  $\mathbf{A}_\alpha$ . Fig. 4c shows the deformed configuration obtained with the skewed mesh.

Bending model	Parameter set	
3D linear elasticity	$E = 480 E_0$	$\nu = 0.38$
Koiter	$\mu = 65.217 E_0 L_0$ $\Lambda = 79.944 E_0 L_0$	$\nu = 0.38$
Helfrich	$k = 4.9308 E_0 L^3$ $\bar{k} = -1.5285 E_0 L^3$ $H_0 = 0$	$\nu = 0.38$
apH	$\mu = 60 E_0 L_0$	$\nu = 0.5$
new	$c_1 = c_2 = 2.4654 E_0 L_0^3$ $c_{12} = 0.9368 E_0 L_0^3$ $c_3 = 0.7643 E_0 L_0^3$	$\nu = 0.38$

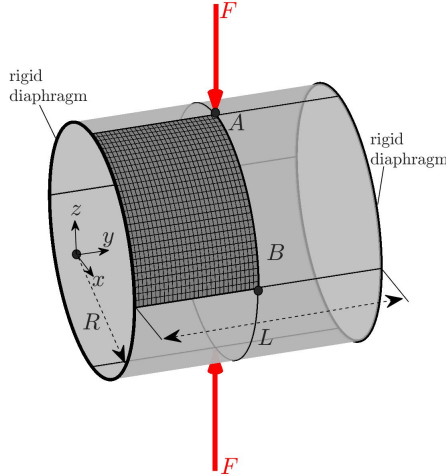
**Table 8:** Simply supported plate: Parameter set used for different bending models according to Eqs. (50), (58) and (69).

## 5.2 Pinched cylindrical shell – linear case

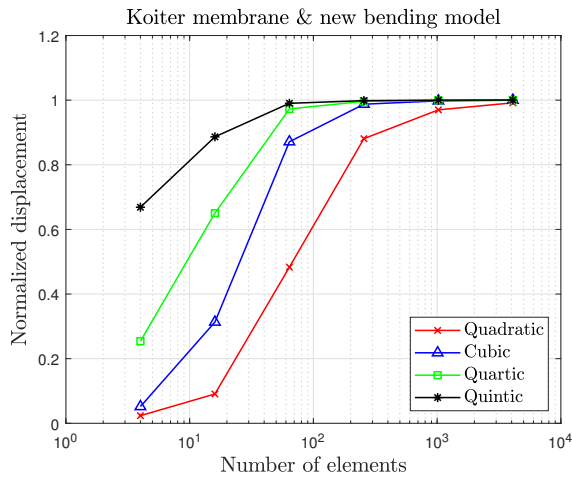
This example analyzes a cylinder with rigid diaphragms at its ends and subjected to point forces as shown in Fig. 5. The cylinder is of dimension  $R = 300L_0$ ,  $L = 600L_0$  and has thickness  $T = 3L_0$ . The rigid diaphragm is realized by fixing the  $x$ - and  $z$ - degrees-of-freedom of the nodes lying at the cylinder ends. The material parameters are Young's modulus  $E = 3E_0$  and Poisson's ratio  $\nu = 0.3$ . The corresponding material parameters for the different bending models are shown in Tab. 9. The magnitude of the two opposing pinching forces is  $F = 10^{-6} E_0 L_0^2$ . Owing to symmetry, the problem is solved for only 1/8 of the cylinder as shown in Fig. 5a. All symmetry conditions are enforced using a penalty method with parameter  $\epsilon = 6 \times 10^2 n_l^{q-1} E_0 L_0^2$  for axial symmetry and  $\epsilon = 6 \times 10^2 n_t^{q-1} E_0 L_0^2$  for circumferential symmetry, where  $n_l$  and  $n_t$  are the number of elements in axial and circumferential directions, respectively. The finite element solution is verified by the analytical solution for the displacement beneath the force from Flügge (1962) and Duong et al. (2017). The proposed bending model converges to the accurate solution as shown in Fig. 5b. Identical convergence behavior is observed for the Koiter and apH model. As the Helfrich bending model is not initially stress-free due to the rear term in Eq. (57.2), highly inaccurate results are obtained for coarse meshes (Fig. 5c).

Bending model	Parameter set	
3D linear elasticity	$E = 3 E_0$	$\nu = 0.3$
Koiter	$\mu = 3.4615 E_0 L_0$ $\Lambda = 2.967 E_0 L_0$	$\nu = 0.3$
Helfrich	$k = 2 c_i = 14.83 E_0 L^3$ $\bar{k} = -5.1923 E_0 L^3$ $H_0 = -0.0016 L_0^{-1}$	$\nu = 0.3$
apH	$\mu = 4.5 E_0 L_0$	$\nu = 0.5$
new	$c_1 = c_2 = 7.4176 E_0 L_0^3$ $c_{12} = 2.2253 E_0 L_0^3$ $c_3 = 2.5962 E_0 L_0^3$	$\nu = 0.3$

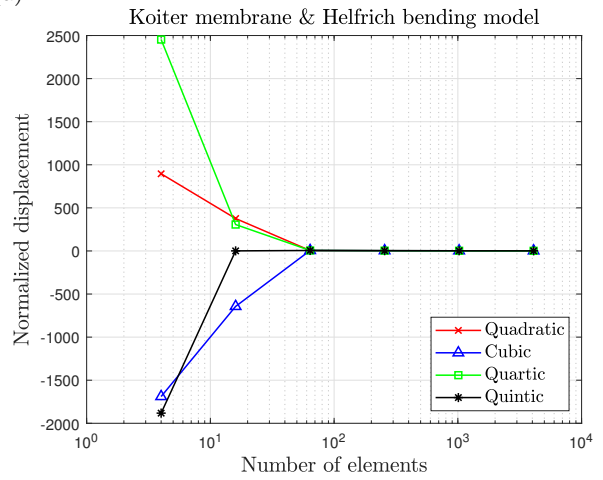
**Table 9:** Pinched cylindrical shell – linear case: Parameter set used for the different bending models according to Eqs. (50), (58) and (69).



(a)



(b)



(c)

**Figure 5:** Pinched cylindrical shell – linear case: (a) Problem setup. Convergence of the displacement beneath the force for the (b) proposed new and (c) Helfrich bending model. The result obtained for the Koiter and apH bending models are similar to those of the proposed new bending model.

### 5.3 Pinched cylindrical shell – nonlinear case

We consider the same problem as in the previous example (see Fig. 5a), but now undergoing large deformations. The radius, length, and thickness of the cylinder now is  $R = 100 L_0$ ,  $L = 200 L_0$ , and  $T = 1.0 L_0$ , respectively. The cylinder is considered to have a Young's modulus  $E = 30 E_0$ , Poisson's ratio  $\nu = 0.3$ . The corresponding bending parameters following from this are tabulated in Tab. 10. Fig. 6a shows the deformed configuration obtained with the point force of  $F = 12 E_0 L_0^2$  applied in 40 loading steps. By employing Lagrange multiplier-based symmetric boundary conditions as in Duong et al. (2017), only 1/8 of the cylinder is used in the FE computations. Fig. 6c presents the force vs. displacement curve (measured at points A and B shown in Fig. 5a) obtained with  $50 \times 50$  quadratic NURBS elements. The reference solution from Sze et al. (2004) is based on Reissner-Mindlin shell elements. The Koiter, Helfrich and new bending models are all in good agreement with the reference solution and thus only the numerical result of the new bending model is shown.

Bending model	Parameter set	
3D linear elasticity	$E = 30 E_0$	$\nu = 0.3$
Koiter	$\mu = 11.538 E_0 L_0$ $\Lambda = 9.8901 E_0 L_0$	$\nu = 0.3$
Helfrich	$k = 5.4945 E_0 L_0^3$ $\bar{k} = -1.9231 E_0 L_0^3$ $H_0 = -0.005 L_0^{-1}$	$\nu = 0.3$
new	$c_1 = c_2 = 2.7473 E_0 L_0^3$ $c_{12} = 0.8242 E_0 L_0^3$ $c_3 = 0.9615 E_0 L_0^3$	$\nu = 0.3$

**Table 10:** Pinched cylindrical shell – nonlinear case: Parameter set used for the different bending models according to Eqs. (50), (58) and (69).

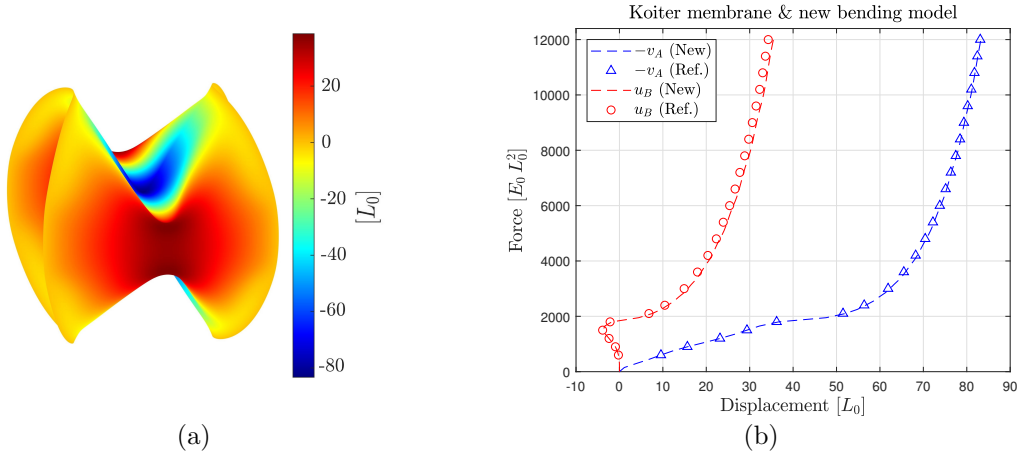


**Figure 6:** Pinched cylindrical shell – nonlinear case: (a) Final configuration colored by the radial displacement. (b) Force-displacement curve for the new bending model. The result obtained for the Koiter and Helfrich bending models are similar to those of the new bending model and hence are omitted here.

The following figures show the membrane stress  $N_\beta^\alpha = N^{\alpha\gamma} a_{\gamma\beta}$  (Fig. 7) and bending stress  $M_\beta^\alpha = M_0^{\alpha\gamma} a_{\gamma\beta}/J$  (Fig. 8), obtained from post-processing based on L2-projection with lumped mass matrix. For  $N_\beta^\alpha$ , only the result of the new bending model is shown as the two other models give similar results. However, for  $M_\beta^\alpha$  the Helfrich model shows distinct differences to both the Koiter and new model. This again shows that the Helfrich model is not able to capture initially stress-free shells properly.

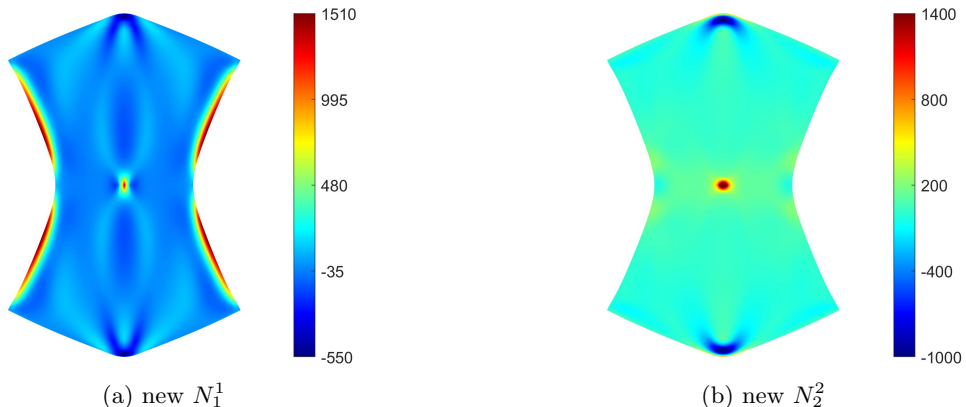


**Figure 7:** Pinched cylindrical shell – nonlinear case: Components of physical membrane stress  $N_\beta^\alpha$  [N/m] for the new bending model.

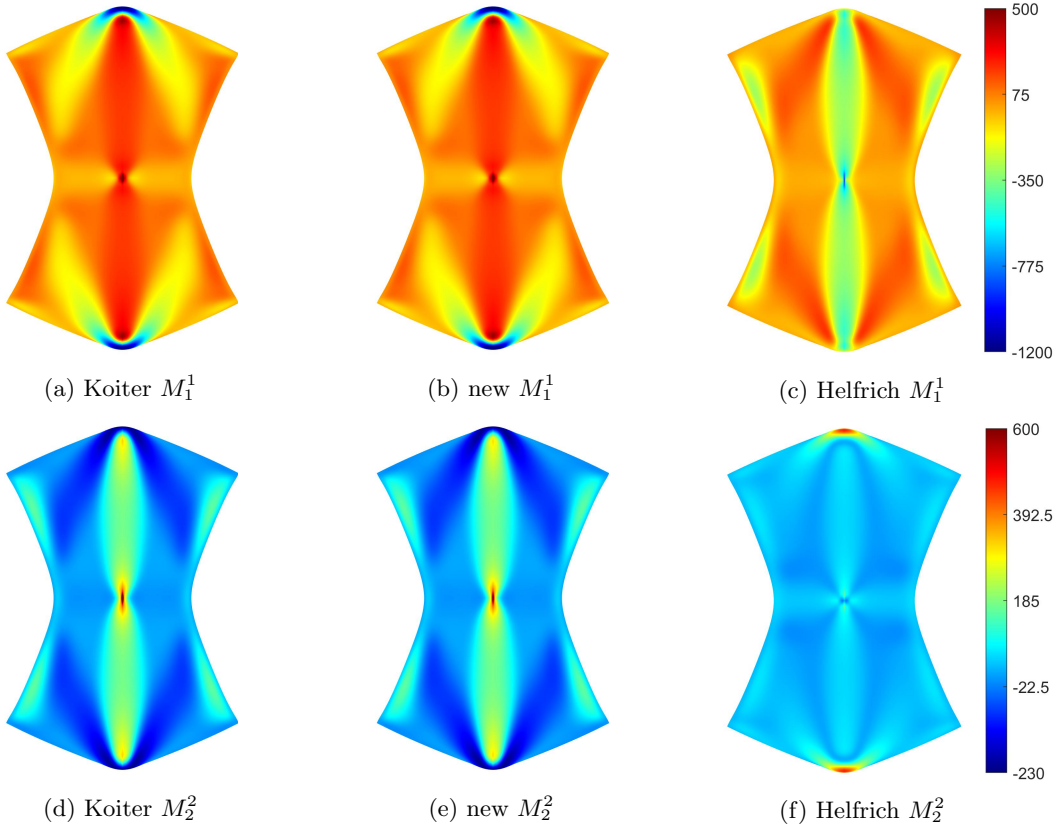


**Figure 8:** Pinched cylindrical shell – nonlinear case: Components of bending stress  $M_\beta^\alpha$  [N]

#### 5.4 Cylindrical shell spreading

Next, we consider an open ended cylinder that is being pulled apart by a pair of opposite forces. The cylinder has dimensions  $R \times L \times T = 4.953 L_0 \times 10.35 L_0 \times 0.094 L_0$ . Only 1/8 of the cylinder is discretized using 20 x 20 NURBS elements as shown in Fig. 9a. The symmetry boundary conditions are enforced via the Lagrange multiplier method of [Duong et al. \(2017\)](#). The bending parameters shown in Tab. 11 are obtained from Young's modulus  $E = 10.5 \times 10^3 E_0$  and Poisson's ratio  $\nu = 0.3125$ . The magnitude of the spreading force is  $F = 40 E_0 L_0^2$  applied in 40 loading steps. Fig. 9c-d shows the force-deflection curve for the new and Helfrich bending models in comparison to the reference solution from [Sze et al. \(2004\)](#). It is evident from these two plots that the Helfrich model again fails to capture the reference solution accurately. As in the previous examples, the solution for the Koiter bending model is similar to that of the new bending model.

Bending model	Parameter set	
3D linear elasticity	$E = 10.5 \times 10^3 E_0$	$\nu = 0.3125$
Koiter	$\mu = 376 E_0 L_0$ $\Lambda = 341.82 E_0 L_0$	$\nu = 0.3123$
Helfrich	$k = 1.6108 E_0 L_0^3$ $\bar{k} = -0.5537 E_0 L_0^3$ $H_0 = -0.1009 L_0^{-1}$	$\nu = 0.3123$
new	$c_1 = c_2 = 0.8054 E_0 L_0^3$ $c_{12} = 0.2517 E_0 L_0^3$ $c_3 = 0.2769 E_0 L_0^3$	$\nu = 0.3125$

**Table 11:** Cylindrical shell spreading: Parameter set used for the different bending models according to Eqs. (50), (58) and (69).

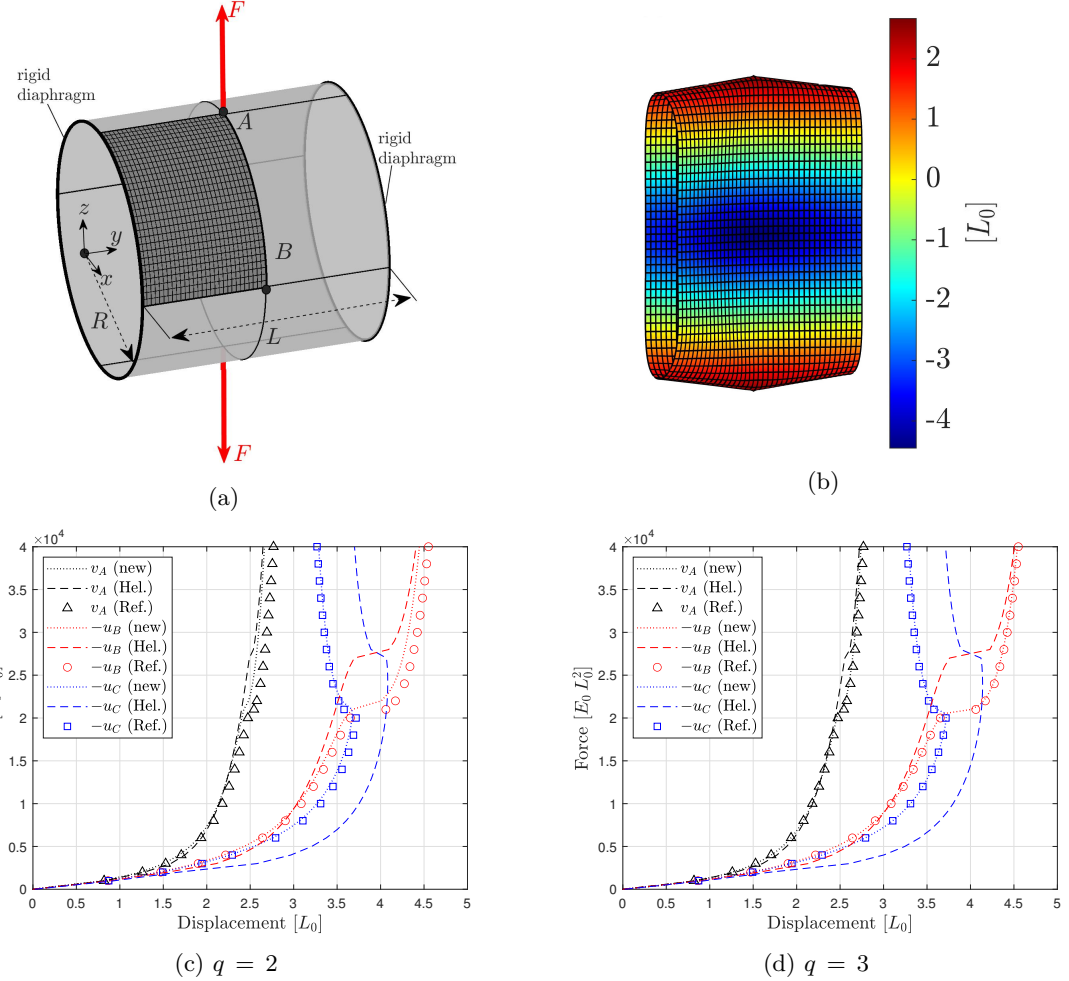


**Figure 9:** Cylindrical shell spreading: (a) problem setup and (b) deformed configuration colored by the radial displacement. Force-displacement curve for FE order (c)  $q = 2$  and (d)  $q = 3$  according to the new model, Helfrich model and reference results of [Sze et al. \(2004\)](#).

## 5.5 Angioplasty simulation

The last example considers contact between an expanding balloon and a tube, which mimics the angioplasty procedure used to clear blocked coronary arteries. The tube has the dimensions  $R_t \times L_t \times T_t = 5 \text{ mm} \times 30 \text{ mm} \times 0.5 \text{ mm}$  and represents a portion of an artery. The balloon within the artery is initially spherical and has the initial radius  $R_b = R_t$  and volume  $V_0 = 4\pi/3R_b^3$ . The tube is modeled using the incompressible Neo-Hookean membrane model from Eq. (59.1) together with either the Koiter or the proposed new bending model using the parameters  $\mu_t = 8 \text{ N/m}$  (corresponding to  $E = 48 \text{ kPa}$  and  $\nu = 0.5$  according to Eq. (50)). The balloon is also modeled by Eq. (59.1) but with  $\mu_b = 5 \mu_t$ . The tube and balloon are discretized using  $n_{el} = 60 \times 55$  and  $n_{el} = 64 \times 32$  quadratic NURBS elements, respectively. The tube and balloon are supported by fixing all normal dofs on the  $x$ -,  $y$ - and  $z$ - symmetry planes. This leaves the tube free to contract longitudinally. The balloon is inflated up to the volume  $V = 3V_0$ . Frictionless contact is enforced using the two-half-pass penalty contact formulation of [Sauer and De Lorenzis \(2013\)](#) with penalty parameter  $\epsilon = 5 E/\text{mm}$ . A similar angioplasty example was studied in [Roohbakhshan and Sauer \(2017, 2018\)](#) using the material model of [Gasser et al. \(2006\)](#).

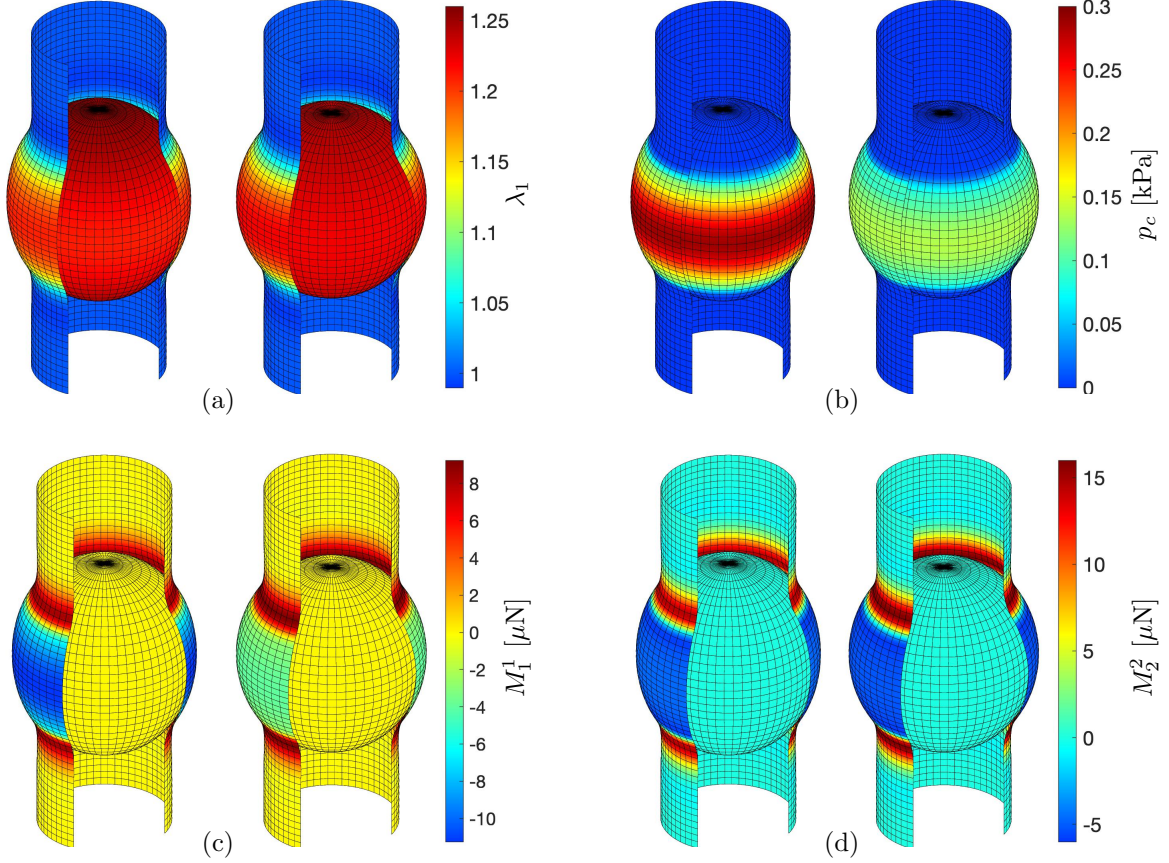


**Figure 10:** Angioplasty simulation: Distribution of (a) Circumferential stretch  $\lambda_1$ , (b) distribution of contact pressure  $p_c$  and, bending moments (c)  $M_1^1$  and (d)  $M_2^2$  at balloon volume  $V = 3V_0$ . In all cases the left figures belong to the Koiter model while the right figures belong to the new bending model. Significant difference between both models appear for  $p_c$  and  $M_1^1$ , but not for  $\lambda_1$  and  $M_2^2$

Fig. 10 shows the deformed configurations of the Koiter (left) and the new (right) bending models colored by different quantities. In Fig. 10a, the deformed configurations are colored by the circumferential stretch  $\lambda_1$ . Though this distribution looks similar, the balloon has slightly higher longitudinal deformation for the Koiter bending model than for the new model, which indicates that the Koiter model is stiffer. This is confirmed by the larger contact pressure  $p_c$  and circumferential bending stress component  $M_1^1$  of the Koiter model shown in Fig. 10b and c, respectively. The longitudinal bending stress component  $M_2^2$ , on the other hand, is again similar for both models as Fig. 10d shows. The large differences between the contact pressure  $p_c$  and moment component  $M_1^1$  can also be seen in Fig. 11. At  $V = 3V_0$ ,  $p_c$  is almost twice as large and  $M_1^1$  almost three times as large for the Koiter than for the new bending model. Up to  $V \approx 1.2V_0$ , however, the differences are small, illustrating once more the equivalency of the two models for small deformations.

Contrary to the previous examples, the angioplasty example thus shows that there are major differences between the Koiter bending model and the proposed new bending model. Those are due to the circumferential stretch in the tube caused by the expanding balloon. In the Koiter model this stretch contributes to the bending moments and stiffness, while it does not in the proposed new model. The effect of bending and stretching can therefore be properly separated in the new model. This was also seen in test case 2 (Sec. 4.2). Since the Koiter bending model reacts to stretches it can be expected to overestimate the bending moments.

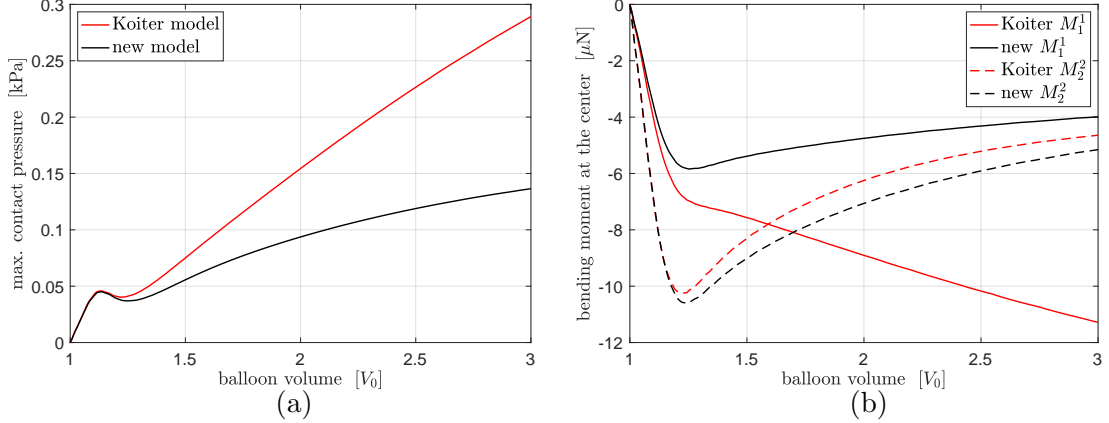


**Figure 11:** Angioplasty simulation: Change in (a) contact pressure ( $p_c$ ) and (b) bending stresses ( $M_1^1$  and  $M_2^2$ ) measured at the center of the tube as a function of increasing balloon volume.

## 6 Conclusion

This work proposes a new bending model for Kirchhoff-Love shells based on the direct surface approach. The proposed bending model eliminates the spurious influence of membrane strains on bending at large deformation. It is objective, can handle initially curved surfaces and large deformations.

The new bending model is introduced in Sec. 3 along with several existing bending models. The relation between the material parameters of the different bending models is provided, and it is shown that all the bending models become equivalent for initially planar shells at small deformations. In contrast to existing bending models, the proposed new model passes an essential set of five elementary bending test cases as was seen in Sec. 4. Test case 1(a) (Sec. 4.1) shows that the Canham and Helfrich models are not initially stress-free. The Helfrich model will be initially stress-free only when one of its bending parameter ( $\bar{k}$ ) is zero. Test case 1(b) considers a final configuration similar to that of a rigid rotation but obtained by counter bending. This test case highlights the anisotropic nature of the new bending model in addition to providing accurate stresses. The Koiter and apH models only partially pass this test due to errors in the Cauchy stress. The Helfrich model fails due to incorrect bending stress and the Canham model fails due to incorrect Cauchy as well as bending stresses. In test case 2(a) (Sec 4.2), a cylinder is inflated, which is a pure membrane action, and hence stresses shouldn't arise from the bending models. The Koiter and apH models partially pass this test with small errors in the bending stresses. The Canham and Helfrich models fail again due to incorrect bending and Cauchy stresses. In test case 2(b), pure bending is considered and all the bending models except the proposed model fail to give zero Cauchy stresses. In test case 3 (Sec 4.3), torsion is considered for which only the Koiter and new bending model are able to provide accurate bending stresses to pass the test.

These observations are confirmed by the five numerical test cases in Sec. 5. In the simply supported linear plate problem (Sec. 5.1), all the bending models considered are identical. This problem is also solved with skew meshes to exhibit that the proposed model gives accurate results also when the principal curvature directions are not aligned with the curvilinear coordinates. The Helfrich model fails in the second linear problem – the pinched cylindrical shell (Sec. 5.2) – due to non-zero initial bending stress. The Helfrich model also deviates from the reference solution for cylinder spreading (Sec. 5.4) for the same reason. Though the Helfrich model gives accurate force vs. displacement for the nonlinear pinching problem (Sec. 5.3), its bending stress

components ( $M_\beta^\alpha$ ) are different from those obtained for the Koiter and the new bending model. Finally in the angioplasty example, the difference between the Koiter and the new model is illustrated. The example shows that bending and stretching can be properly separated in the new model, which is not the case for the Koiter model where it results in much larger bending moments.

The proposed new model is able to circumvent problems in existing bending models by using stretch-invariant bending quantities. It serves as a bending model with an union of desired features for shell models in the direct surface approach. As the model is based on the principal curvature directions and has four different material parameters, it provides flexibility in modeling new materials. In future, it would be interesting to combine the new bending model with anisotropic membrane models based on the Mooney–Rivlin (Mooney, 1940; Rivlin and Saunders, 1951) and Gasser–Ogden–Holzapfel model for biological tissues (Gasser et al., 2006).

## Acknowledgements

The authors are grateful to the Deutsche Forschungsgemeinschaft (DFG, German Research Foundation) – 333849990/GRK2379 (IRTG Modern Inverse Problems) for supporting this research. The authors also wish to thank Farshad Roohbakhshan for his help with the numerical examples.

## A Material tangents of the proposed model

For the proposed model, the fourth order material tensor components defined in Eq. (30) are

$$\begin{aligned} c^{\alpha\beta\gamma\delta} &= \ell_{11}^{\alpha\beta} \ell_{11}^{\gamma\delta} \left[ c_1 \kappa_1 \left( 4\kappa_1 - \frac{3\kappa_{01}}{\lambda_1} \right) + \frac{3c_{12}\kappa_1}{\lambda_1} k_2 + c_3 \left( \frac{3\kappa_{12}^2\lambda_2}{2\lambda_1} - \frac{5\kappa_{012}\kappa_{12}\sqrt{\lambda_2}}{4\lambda_1^{3/2}} \right) \right] \\ &+ \ell_{22}^{\alpha\beta} \ell_{22}^{\gamma\delta} \left[ c_2 \kappa_2 \left( 4\kappa_2 - \frac{3\kappa_{02}}{\lambda_2} \right) + \frac{3c_{12}\kappa_2}{\lambda_2} k_1 + c_3 \left( \frac{3\kappa_{12}^2\lambda_1}{2\lambda_2} - \frac{5\kappa_{012}\kappa_{12}\sqrt{\lambda_1}}{4\lambda_2^{3/2}} \right) \right] \\ &+ (\ell_{11}^{\alpha\beta} \ell_{22}^{\gamma\delta} + \ell_{22}^{\alpha\beta} \ell_{11}^{\gamma\delta}) \left[ c_{12} \kappa_1 \kappa_2 + c_3 \left( \frac{\kappa_{12}^2}{2} - \frac{\kappa_{012}\kappa_{12}}{4\sqrt{\lambda_1\lambda_2}} \right) \right], \end{aligned} \quad (125)$$

$$\begin{aligned} d^{\alpha\beta\gamma\delta} &= \ell_{11}^{\alpha\beta} \ell_{11}^{\gamma\delta} \left[ c_1 \left( \frac{\kappa_{01}}{\lambda_1} - \kappa_1 \right) + \frac{c_{12}}{\lambda_1} (\kappa_{02} - \lambda_2 \kappa_2) \right] - c_{12} \ell_{11}^{\alpha\beta} \ell_{22}^{\gamma\delta} \kappa_1 \\ &+ \ell_{22}^{\alpha\beta} \ell_{22}^{\gamma\delta} \left[ c_2 \left( \frac{\kappa_{02}}{\lambda_2} - \kappa_2 \right) + \frac{c_{12}}{\lambda_2} (\kappa_{01} - \lambda_1 \kappa_1) \right] - c_{12} \ell_{22}^{\alpha\beta} \ell_{11}^{\gamma\delta} \kappa_2 \\ &+ \frac{c_3}{2\sqrt{\lambda_1\lambda_2}} \left( \frac{\kappa_{012}}{\sqrt{\lambda_1\lambda_2}} - 2\kappa_{12} \right) (\lambda_2 \ell_{11}^{\alpha\beta} + \lambda_1 \ell_{22}^{\alpha\beta}) \ell_{12}^{\gamma\delta}, \end{aligned} \quad (126)$$

$$e^{\alpha\beta\gamma\delta} = d^{\gamma\delta\alpha\beta}, \quad (127)$$

$$f^{\alpha\beta\gamma\delta} = \ell_{11}^{\alpha\beta} \ell_{11}^{\gamma\delta} c_1 + \ell_{22}^{\alpha\beta} \ell_{22}^{\gamma\delta} c_2 + (\ell_{22}^{\alpha\beta} \ell_{11}^{\gamma\delta} + \ell_{11}^{\alpha\beta} \ell_{22}^{\gamma\delta}) c_{12} + \ell_{12}^{\alpha\beta} \ell_{12}^{\gamma\delta} c_3. \quad (128)$$

The tensor components corresponding to the bending models of Koiter, projected Neo-Hooke, and Canham and Helfrich can be found in Duong et al. (2017), Roohbakhshan and Sauer (2017) and Sauer and Duong (2017), respectively.

## B Efficient FE implementation

If the initial principal curvature directions align with surface tangents ( $\mathbf{A}_\alpha$ ), then the quantity defined in Eq. (66) will be

$$L_i^\alpha = \frac{\delta_i^\alpha}{\sqrt{A_{ii}}}, \quad (\text{no summation on } i). \quad (129)$$

The stretches along those direction will then simply be,

$$\lambda_1 = \sqrt{\frac{a_{11}}{A_{11}}}, \quad \lambda_2 = \sqrt{\frac{a_{22}}{A_{22}}}. \quad (130)$$

Plugging this into the quantities of Eq. (68) leads to

$$\begin{aligned} [l_{11}^{\alpha\beta}] &= \frac{1}{\mathcal{A}_1} \begin{bmatrix} 1 & 0 \\ 0 & 0 \end{bmatrix}, \quad [l_{22}^{\alpha\beta}] = \frac{1}{\mathcal{A}_2} \begin{bmatrix} 0 & 0 \\ 0 & 1 \end{bmatrix}, \\ [l_{12}^{\alpha\beta}] &= \frac{1}{\sqrt{\mathcal{A}_1 \mathcal{A}_2}} \begin{bmatrix} 0 & 1 \\ 1 & 0 \end{bmatrix}, \end{aligned} \quad (131)$$

where

$$\mathcal{A}_1 := \sqrt{A_{11} a_{11}}, \quad \mathcal{A}_2 := \sqrt{A_{22} a_{22}}. \quad (132)$$

Using this simplification, the stress and moment can be directly calculated as

$$\tau^{11} = - \left( c_1 k_1 + c_{12} k_2 + \frac{c_3 \sqrt{\lambda_2} \kappa_{12} k_{12}}{2 \sqrt{\lambda_1}} \right) \frac{\kappa_1}{\mathcal{A}_1}, \quad (133)$$

$$\tau^{22} = - \left( c_{12} k_1 + c_2 k_2 + \frac{c_3 \sqrt{\lambda_1} \kappa_{12} k_{12}}{2 \sqrt{\lambda_2}} \right) \frac{\kappa_2}{\mathcal{A}_2}, \quad (134)$$

$$\tau^{12} = \tau^{21} = 0, \quad (135)$$

$$M_0^{11} = (c_1 k_1 + c_{12} k_2) \frac{1}{\mathcal{A}_1}, \quad (136)$$

$$M_0^{22} = (c_{12} k_1 + c_2 k_2) \frac{1}{\mathcal{A}_2}, \quad (137)$$

$$M_0^{12} = M_0^{21} = \frac{c_3 k_{12}}{\sqrt{\mathcal{A}_1 \mathcal{A}_2}}. \quad (138)$$

As described in Duong et al. (2017), for the efficient computation of the FE stiffness matrices we can exploit the symmetries to rearrange the fourth order tensor,  $f^{\alpha\beta\gamma\delta}$  as

$$\mathbf{F} := \begin{bmatrix} f^{1111} & f^{1122} & f^{1112} \\ f^{2211} & f^{2222} & f^{2212} \\ f^{1211} & f^{1222} & f^{1212} \end{bmatrix}. \quad (139)$$

Based on the simplification in Eq (131), this rearrangement simplifies to

$$\mathbf{F} := \begin{bmatrix} \frac{c_1}{(\mathcal{A}_1)^2} & \frac{c_{12}}{\mathcal{A}_1 \mathcal{A}_2} & 0 \\ \frac{c_{12}}{\mathcal{A}_1 \mathcal{A}_2} & \frac{c_2}{(\mathcal{A}_2)^2} & 0 \\ 0 & 0 & \frac{c_3}{\mathcal{A}_1 \mathcal{A}_2} \end{bmatrix}. \quad (140)$$

Similar rearrangement can be applied to  $c^{\alpha\beta\gamma\delta}$ ,  $d^{\alpha\beta\gamma\delta}$  and  $e^{\alpha\beta\gamma\delta}$ . Further, we define the auxiliary terms

$$\begin{aligned}\mathbf{L}_{\alpha\beta}^a &:= \mathbf{N}_{,\alpha}^T \mathbf{a}_\beta, \\ \mathbf{L}_\alpha^n &:= \mathbf{N}_{,\alpha}^T \mathbf{n}, \\ \mathbf{G}_{\alpha\beta}^n &:= \tilde{\mathbf{N}}_{;\alpha\beta}^T \mathbf{n},\end{aligned}\quad (141)$$

where each term is an array of size  $(3n \times 1)$ , with  $n$  being the number of control points per element. This is further reorganized as

$$\hat{\mathbf{L}}_a = [\mathbf{L}_{11}^a, \mathbf{L}_{22}^a, \mathbf{L}_{12}^a + \mathbf{L}_{21}^a], \quad (142)$$

$$\hat{\mathbf{G}}_n = [\mathbf{G}_{11}^n, \mathbf{G}_{22}^n, \mathbf{G}_{12}^n + \mathbf{G}_{21}^n]. \quad (143)$$

We can then rewrite the equations for force,

$$\mathbf{f}_{\text{int}\tau}^e = \int_{\Omega_0^e} \hat{\mathbf{L}}_a \hat{\boldsymbol{\tau}} \, dA, \quad (144)$$

$$\mathbf{f}_{\text{int}M}^e = \int_{\Omega_0^e} \hat{\mathbf{G}}_n \hat{\mathbf{M}}_0 \, dA, \quad (145)$$

material stiffness,

$$\mathbf{k}_{\tau\tau}^e = \int_{\Omega_0^e} \hat{\mathbf{L}}_a \mathbf{C} \hat{\mathbf{L}}_a^T \, dA, \quad (146)$$

$$\mathbf{k}_{\tau M}^e = \int_{\Omega_0^e} \hat{\mathbf{L}}_a \mathbf{D} \hat{\mathbf{G}}_n^T \, dA, \quad (147)$$

$$\mathbf{k}_{M\tau}^e = \int_{\Omega_0^e} \hat{\mathbf{G}}_n \mathbf{E} \hat{\mathbf{L}}_a^T \, dA, \quad (148)$$

$$\mathbf{k}_{MM}^e = \int_{\Omega_0^e} \hat{\mathbf{G}}_n \mathbf{F} \hat{\mathbf{G}}_n^T \, dA, \quad (149)$$

and geometric stiffness,

$$\mathbf{k}_{M1}^e = - \int_{\Omega_0^e} b_M (a^{11} \mathbf{L}_1^n \mathbf{L}_1^{nT} + a^{22} \mathbf{L}_2^n \mathbf{L}_2^{nT} + a^{12} (\mathbf{L}_1^n \mathbf{L}_2^{nT} + \mathbf{L}_2^n \mathbf{L}_1^{nT})) \, dA, \quad (150)$$

$$\mathbf{k}_{M2}^e = - \int_{\Omega_0^e} (\mathbf{L}_1^n \mathbf{a}^{1T} + \mathbf{L}_2^n \mathbf{a}^{2T}) (M_0^{11} \tilde{\mathbf{N}}_{;11} + M_0^{22} \tilde{\mathbf{N}}_{;22} + 2 M_0^{12} \tilde{\mathbf{N}}_{;12}) \, dA. \quad (151)$$

Where

$$\begin{aligned}\hat{\boldsymbol{\tau}} &:= [\tau^{11}, \tau^{22}, \tau^{12}]^T, \\ \hat{\mathbf{M}}_0 &:= [M_0^{11}, M_0^{22}, M_0^{12}]^T, \\ \hat{\mathbf{b}} &:= [b_{11}, b_{22}, 2b_{12}]^T, \\ b_M &:= \hat{\mathbf{b}}^T \hat{\mathbf{M}}_0.\end{aligned}\quad (152)$$

## C Bending moduli extraction

In order to calculate the bending moduli of the new bending model we directly compare the values of  $f^{\alpha\beta\gamma\delta}$  in (40) for the Koiter model and the new bending model. For the Koiter model, the fourth order tensor is given by

$$f_{\text{Koi}}^{\alpha\beta\gamma\delta} = \frac{T^2}{12} (\Lambda A^{\alpha\beta} A^{\gamma\delta} + \mu (A^{\alpha\gamma} A^{\beta\delta} + A^{\alpha\delta} A^{\beta\gamma})). \quad (153)$$

Choosing a parametrization with  $A_{12} = A_{21} = 0$  and noting that  $f^{\alpha\beta\gamma\delta}$  has major and minor symmetries, the tensor can be represented only by the following elements

$$\begin{aligned} f_{\text{Koi}}^{1111} &= \frac{T^2 (\Lambda + 2\mu)}{12 \|\mathbf{A}_1\|^4}, & f_{\text{Koi}}^{2211} &= \frac{T^2 \Lambda}{12 (\|\mathbf{A}_1\|^2 \|\mathbf{A}_2\|^2)}, & f_{\text{Koi}}^{1211} &= 0, \\ f_{\text{Koi}}^{1122} &= \frac{T^2 \Lambda}{12 (\|\mathbf{A}_1\|^2 \|\mathbf{A}_2\|^2)}, & f_{\text{Koi}}^{2222} &= \frac{T^2 (\Lambda + 2\mu)}{12 \|\mathbf{A}_1\|^4}, & f_{\text{Koi}}^{1222} &= 0, \\ f_{\text{Koi}}^{1112} &= 0, & f_{\text{Koi}}^{2212} &= 0, & f_{\text{Koi}}^{1212} &= \frac{T^2 \mu}{12 (\|\mathbf{A}_1\|^2 \|\mathbf{A}_2\|^2)}. \end{aligned} \quad (154)$$

The corresponding fourth order tensor components for the new model are of the form

$$\begin{aligned} f_{\text{new}}^{\alpha\beta\gamma\delta} &= \sum_{i=1}^2 \frac{c_i}{\lambda_i^2} L_i^\alpha L_i^\beta L_i^\gamma L_i^\delta + \frac{c_{12}}{\lambda_1 \lambda_2} \left( L_1^\alpha L_1^\beta L_2^\gamma L_2^\delta + L_2^\alpha L_2^\beta L_1^\gamma L_1^\delta \right) \\ &\quad \frac{c_3}{\lambda_1 \lambda_2} \left( L_1^\alpha L_2^\beta + L_2^\alpha L_1^\beta \right) \left( L_1^\gamma L_2^\delta + L_2^\gamma L_1^\delta \right). \end{aligned} \quad (155)$$

The way  $L_i^\alpha$  is calculated in the numerical examples is by using

$$L_i^\alpha = \frac{\mathbf{A}_i}{\|\mathbf{A}_i\|} \cdot \mathbf{A}^\alpha, \quad (156)$$

for a particular choice of parametrization. Thus only  $L_1^1$  and  $L_2^2$  will be non-zero. So by considering  $\lambda_i = 1$ ,

$$\begin{aligned} f_{\text{new}}^{1111} &= \frac{c_1}{\|\mathbf{A}_1\|^4}, & f_{\text{new}}^{2211} &= \frac{c_{12}}{\|\mathbf{A}_1\|^2 \|\mathbf{A}_2\|^2}, & f_{\text{new}}^{1211} &= 0, \\ f_{\text{new}}^{1122} &= \frac{c_{12}}{\|\mathbf{A}_1\|^2 \|\mathbf{A}_2\|^2}, & f_{\text{new}}^{2222} &= \frac{c_2}{\|\mathbf{A}_1\|^4}, & f_{\text{new}}^{1222} &= 0, \\ f_{\text{new}}^{1112} &= 0, & f_{\text{new}}^{2212} &= 0, & f_{\text{new}}^{1212} &= \frac{c_3}{\|\mathbf{A}_1\|^2 \|\mathbf{A}_2\|^2}. \end{aligned} \quad (157)$$

Comparing Eqs. (154) and Eqs. (157), then leads to Eq. (69).

## References

Adam, C., Bouabdallah, S., Zarroug, M., and Maitournam, H. (2015). Improved numerical integration for locking treatment in isogeometric structural elements. part II: Plates and shells. *Computer Methods in Applied Mechanics and Engineering*, **284**:106–137. Isogeometric Analysis Special Issue.

Ahmad, S., Irons, B. M., and Zienkiewicz, O. (1970). Analysis of thick and thin shell structures by curved finite elements. *International Journal for Numerical Methods in Engineering*, **2**(3):419–451.

Auddya, D., Zhang, X., Gulati, R., Vasan, R., Garikipati, K., Rangamani, P., and Rudraraju, S. (2021). Biomembranes undergo complex, non-axisymmetric deformations governed by Kirchhoff–Love kinematics and revealed by a three-dimensional computational framework. *Proceedings of the Royal Society A*, **477**(2255):20210246.

Bartezzaghi, A., Dedè, L., and Quarteroni, A. (2019). Biomembrane modeling with isogeometric analysis. *Computer Methods in Applied Mechanics and Engineering*, **347**:103–119.

Başar, Y. and Itskov, M. (1998). Finite element formulation of the Ogden material model with application to rubber-like shells. *International Journal for Numerical Methods in Engineering*, **42**(7):1279–1305.

Benson, D., Bazilevs, Y., Hsu, M.-C., and Hughes, T. (2010). Isogeometric shell analysis: the reissner–mindlin shell. *Computer Methods in Applied Mechanics and Engineering*, **199**(5–8):276–289.

Betsch, P., Gruttmann, F., and Stein, E. (1996). A 4-node finite shell element for the implementation of general hyperelastic 3D-elasticity at finite strains. *Computer Methods in Applied Mechanics and Engineering*, **130**(1-2):57–79.

Bieber, S., Oesterle, B., Ramm, E., and Bischoff, M. (2018). A variational method to avoid locking—Independent of the discretization scheme. *International Journal for Numerical Methods in Engineering*, **114**(8):801–827.

Bischoff, M., Bletzinger, K.-U., Wall, W. A., and Ramm, E. (2004). Models and finite elements for thin-walled structures. In *Encyclopedia of Computational Mechanics*, chapter 3. Wiley & Sons, Ltd, New York.

Borden, M. J., Scott, M. A., Evans, J. A., and Hughes, T. J. R. (2011). Isogeometric finite element data structures based on Bézier extraction of NURBS. *International Journal for Numerical Methods in Engineering*, **87**(1-5):15–47.

Borzeszkowski, B., Lubowiecka, I., and Sauer, R. A. (2022). Nonlinear material identification of heterogeneous isogeometric Kirchhoff–Love shells. *Computer Methods in Applied Mechanics and Engineering*, **390**:114442.

Brunet, M. and Sabourin, F. (2006). Analysis of a rotation-free 4-node shell element. *International Journal for Numerical Methods in Engineering*, **66**(9):1483–1510.

Canham, P. (1970a). The minimum energy of bending as a possible explanation of the biconcave shape of the human red blood cell. *Journal of Theoretical Biology*, **26**(1):61–81.

Canham, P. B. (1970b). The minimum energy of bending as a possible explanation of the biconcave shape of the human red blood cell. *Journal of Theoretical Biology*, **26**(1):61–81.

Caseiro, J., Valente, R. F., Reali, A., Kiendl, J., Auricchio, F., and Alves de Sousa, R. (2014). On the assumed natural strain method to alleviate locking in solid-shell NURBS-based finite elements. *Computational Mechanics*, **53**(6):1341–1353.

Casquero, H., Bona-Casas, C., and Gomez, H. (2017). NURBS-based numerical proxies for red blood cells and circulating tumor cells in microscale blood flow. *Computer Methods in Applied Mechanics and Engineering*, **316**:646–667. Special Issue on Isogeometric Analysis: Progress and Challenges.

Chróścielewski, J., Makowski, J., and Stumpf, H. (1992). Genuinely resultant shell finite elements accounting for geometric and material non-linearity. *International Journal for Numerical Methods in Engineering*, **35**(1):63–94.

Ciarlet, P. G. (2005). An introduction to differential geometry with applications to elasticity. *Journal of Elasticity*, **78**(1):1–215.

Cicala, P. (1965). *Systematic approximation approach to linear shell theory*. Libreria Editrice Universitaria Levrotto & Bella.

Cosserat, E. (1909). In Cosserat F. *Theorie des corps deformables, Paris, Hermann.*

Dao, M., Lim, C., and Suresh, S. (2003). Mechanics of the human red blood cell deformed by optical tweezers. *Journal of the Mechanics and Physics of Solids*, **51**(11):2259–2280. Proceedings of a Symposium on Dynamic Failure and Thin Film Mechanics, honoring Professor L.B. Freund.

Dortdivanlioglu, B. and Javili, A. (2021). Boundary viscoelasticity theory at finite deformations and computational implementation using isogeometric analysis. *Computer Methods in Applied Mechanics and Engineering*, **374**:113579.

Duong, T. X., Khiêm, V. N., Itskov, M., and Sauer, R. A. (2020). A general theory for anisotropic Kirchhoff-Love shells with embedded fibers and in-plane bending. *arXiv preprint arXiv:2101.03122*.

Duong, T. X., Roohbakhshan, F., and Sauer, R. A. (2017). A new rotation-free isogeometric thin shell formulation and a corresponding continuity constraint for patch boundaries. *Computer Methods in Applied Mechanics and Engineering*, **316**:43–83.

Dvorkin, E. N. and Bathe, K.-J. (1984). A continuum mechanics based four-node shell element for general non-linear analysis. *Engineering Computations*, **1**:77–88.

Elguedj, T. and Hughes, T. (2014). Isogeometric analysis of nearly incompressible large strain plasticity. *Computer Methods in Applied Mechanics and Engineering*, **268**:388–416.

Ericksen, J. and Truesdell, C. (1957). Exact theory of stress and strain in rods and shells. *Archive for Rational Mechanics and Analysis*, **1**(1):295–323.

Evans, E. and Hochmuth, R. (1976). Membrane viscoelasticity. *Biophysical Journal*, **16**(1):1–11.

Feng, F. and Klug, W. S. (2006). Finite element modeling of lipid bilayer membranes. *Journal of Computational Physics*, **220**(1):394–408.

Flügge, W. (1962). *Stresses in shells*. Springer-Verlag.

Gasser, T. C., Ogden, R. W., and Holzapfel, G. A. (2006). Hyperelastic modelling of arterial layers with distributed collagen fibre orientations. *Journal of The Royal Society Interface*, **3**(6):15–35.

Gol'denveizer, A. (1963). Derivation of an approximate theory of shells by means of asymptotic integration of the equations of the theory of elasticity. *Journal of Applied Mathematics and Mechanics*, **27**(4):903–924.

Green, A. E., Naghdi, P. M., and Wainwright, W. (1965). A general theory of a Cosserat surface. *Archive for Rational Mechanics and Analysis*, **20**(4):287–308.

Helfrich, W. (1973). Elastic properties of lipid bilayers: theory and possible experiments. *Zeitschrift für Naturforschung c*, **28**(11-12):693–703.

Hughes, T. J. (2012). *The finite element method: linear static and dynamic finite element analysis*. Courier Corporation.

Hughes, T. J., Cottrell, J. A., and Bazilevs, Y. (2005). Isogeometric analysis: CAD, finite elements, nurbs, exact geometry and mesh refinement. *Computer Methods in Applied Mechanics and Engineering*, **194**(39-41):4135–4195.

Hughes, T. J. and Liu, W. K. (1981). Nonlinear finite element analysis of shells: Part I. three-dimensional shells. *Computer Methods in Applied Mechanics and Engineering*, **26**(3):331–362.

Itskov, M. (2001). A generalized orthotropic hyperelastic material model with application to incompressible shells. *International Journal for Numerical Methods in Engineering*, **50**(8):1777–1799.

Kiendl, J., Bletzinger, K.-U., Linhard, J., and Wüchner, R. (2009). Isogeometric shell analysis with Kirchhoff–Love elements. *Computer Methods in Applied Mechanics and Engineering*, **198**(49-52):3902–3914.

Kiendl, J., Hsu, M.-C., Wu, M. C., and Reali, A. (2015). Isogeometric Kirchhoff–Love shell formulations for general hyperelastic materials. *Computer Methods in Applied Mechanics and Engineering*, **291**:280–303.

Kiendl, J., Schmidt, R., Wüchner, R., and Bletzinger, K.-U. (2014). Isogeometric shape optimization of shells using semi-analytical sensitivity analysis and sensitivity weighting. *Computer Methods in Applied Mechanics and Engineering*, **274**:148–167.

Kirchhoff, G. (1850). Ueber die Schwingungen einer kreisförmigen elastischen Scheibe. *Annalen der Physik*, **157**(10):258–264.

Koiter, W. T. (1966). On the nonlinear theory of thin elastic shells. *Proc. Koninkl. Ned. Akad. van Wetenschappen, Series B*, **69**:1–54.

Krysl, P. and Belytschko, T. (1996). Analysis of thin shells by the element-free Galerkin method. *International Journal of Solids and Structures*, **33**(20):3057–3080.

Landau, L. D. and Lifshitz, E. M. (1986). *Course of Theoretical Physics, Theory of Elasticity*, vol. 7. Pergamon Press, Oxford.

Love, A. E. H. (1888). XVI. The small free vibrations and deformation of a thin elastic shell. *Philosophical Transactions of the Royal Society of London. (A.)*, **(179)**:491–546.

Mills, J., Qie, L., Dao, M., Lim, C., and Suresh, S. (2004). Nonlinear elastic and viscoelastic deformation of the human red blood cell with optical tweezers. *Molecular & Cellular Biomechanics*, **1**(3):169.

Mindlin, R. (1951). Influence of rotatory inertia and shear on flexural motions of isotropic, elastic plates. *Journal of Applied Mechanics*, **18**:31–38.

Mooney, M. (1940). A theory of large elastic deformation. *Journal of applied physics*, **11**(9):582–592.

Naghdi, P. M. (1973). The theory of shells and plates. In *Linear Theories of Elasticity and Thermoelasticity*, pages 425–640. Springer, Berlin, Heidelberg.

Neff, P. (2005). A geometrically exact viscoplastic membrane-shell with viscoelastic transverse shear resistance avoiding degeneracy in the thin-shell limit. *Zeitschrift für angewandte Mathematik und Physik ZAMP*, **56**(1):148–182.

Noels, L. and Radovitzky, R. (2008). A new discontinuous Galerkin method for Kirchhoff–Love shells. *Computer Methods in Applied Mechanics and Engineering*, **197**(33):2901–2929.

Novozhilov, V. (1953). Foundations of the nonlinear theory of elasticity. *Bull. Amer. Math. Soc.*, **59**:467–473.

Oñate, E. and Zárate, F. (2000). Rotation-free triangular plate and shell elements. *International Journal for Numerical Methods in Engineering*, 47(1-3):557–603.

Pandolfi, A. and Manganiello, F. (2006). A model for the human cornea: constitutive formulation and numerical analysis. *Biomechanics and Modeling in Mechanobiology*, 5(4):237–246.

Paul, K. and Sauer, R. A. (2022). An isogeometric finite element formulation for surface and shell viscoelasticity based on a multiplicative surface deformation split. *International Journal for Numerical Methods in Engineering*.

Pietraszkiewicz, W. (1989). Geometrically nonlinear theories of thin elastic shells. *Advances in Mechanics*, 12:51–130.

Prot, V., Skallerud, B., and Holzapfel, G. (2007). Transversely isotropic membrane shells with application to mitral valve mechanics. constitutive modelling and finite element implementation. *International Journal for Numerical Methods in Engineering*, 71(8):987–1008.

Reissner, E. (1945). The effect of transverse shear deformation on the bending of elastic plates.

Reissner, E. (1963). On the derivation of the theory of thin elastic shells. *Journal of Mathematics and Physics*, 42(1-4):263–277.

Rivlin, R. S. and Saunders, D. W. (1951). Large elastic deformations of isotropic materials VII. experiments on the deformation of rubber. *Philosophical Transactions of the Royal Society of London. Series A, Mathematical and Physical Sciences*, 243(865):251–288.

Roohbakhshan, F. and Sauer, R. A. (2017). Efficient isogeometric thin shell formulations for soft biological materials. *Biomechanics and Modeling in Mechanobiology*, 16(5):1569–1597.

Roohbakhshan, F. and Sauer, R. A. (2018). Simulation of angioplasty using isogeometric laminated composite shell elements. *PAMM*, 18(1):e201800327.

Sauer, R. A. (2018). On the computational modeling of lipid bilayers using thin-shell theory. In D. Steigmann (Ed.), *The role of mechanics in the study of lipid bilayers*, pages 221–286. Springer, Cham.

Sauer, R. A. and De Lorenzis, L. (2013). A computational contact formulation based on surface potentials. *Computer Methods in Applied Mechanics and Engineering*, 253:369–395.

Sauer, R. A. and Duong, T. X. (2017). On the theoretical foundations of thin solid and liquid shells. *Mathematics and Mechanics of Solids*, 22(3):343–371.

Sauer, R. A., Duong, T. X., and Corbett, C. J. (2014). A computational formulation for constrained solid and liquid membranes considering isogeometric finite elements. *Computer Methods in Applied Mechanics and Engineering*, 271:48–68.

Sauer, R. A., Duong, T. X., Mandadapu, K. K., and Steigmann, D. J. (2017). A stabilized finite element formulation for liquid shells and its application to lipid bilayers. *Journal of Computational Physics*, 330:436–466.

Simo, J. C., Fox, D. D., and Rifai, M. S. (1990). On a stress resultant geometrically exact shell model. Part III: Computational aspects of the nonlinear theory. *Computer Methods in Applied Mechanics and Engineering*, 79(1):21–70.

Steigmann, D. (1999). Fluid films with curvature elasticity. *Archive for Rational Mechanics and Analysis*, 150(2):127–152.

Steigmann, D. (2018). Equilibrium of elastic lattice shells. *Journal of Engineering Mathematics*, **109**(1):47–61.

Steigmann, D. J. (2012). Extension of Koiter’s linear shell theory to materials exhibiting arbitrary symmetry. *International Journal of Engineering Science*, **51**:216–232.

Steigmann, D. J. (2013). Koiter’s shell theory from the perspective of three-dimensional nonlinear elasticity. *Journal of Elasticity*, **111**(1):91–107.

Sze, K., Liu, X., and Lo, S. (2004). Popular benchmark problems for geometric nonlinear analysis of shells. *Finite Elements in Analysis and Design*, **40**(11):1551–1569.

Taylor, R. L. (2011). Isogeometric analysis of nearly incompressible solids. *International Journal for Numerical Methods in Engineering*, **87**(1-5):273–288.

Tepole, A. B., Kabaria, H., Bletzinger, K.-U., and Kuhl, E. (2015). Isogeometric Kirchhoff–Love shell formulations for biological membranes. *Computer Methods in Applied Mechanics and Engineering*, **293**:328–347.

Ugural, A. C. (2009). *Stresses in beams, plates, and shells*. CRC press.

Zou, Z., Hughes, T., Scott, M., Sauer, R., and Savitha, E. (2021). Galerkin formulations of isogeometric shell analysis: Alleviating locking with Greville quadratures and higher-order elements. *Computer Methods in Applied Mechanics and Engineering*, **380**:113757.